Keratin-derived functional carbon with superior charge storage and transport for high-performance supercapacitors

Prerna Sinha[a], Amit Yadav[a], Alekha Tyagi[a], Pradip Paik[b], Hiroyuki Yokoi[c], Amit K. Naskar[d], Tapas Kuila[e], Kamal K. Kar[a,f]

[a]Advanced Nanoengineering Materials Laboratory, Materials Science Programme, Indian Institute of Technology Kanpur, Kanpur, 208016, India

[b]School of Biomedical Engineering, Indian Institute of Technology BHU, Varanasi, Uttar Pradesh, 221005, India

[c]Nanocarbon Materials Science Lab, Advanced Science and Technology, Kumamoto University, Kumamoto, 860-8555, Japan

[d]Chemical Sciences Division, Oak Ridge National Laboratory, Oak Ridge, TN, 37831-6053, USA

[e]Surface Engineering & Tribology Group, CSIR-Central Mechanical Engineering Research Institute, M. G. Avenue, Durgapur, 713 209, India

[f]Advanced Nanoengineering Materials Laboratory, Department of Mechanical Engineering, Indian Institute of Technology Kanpur, Kanpur, 208016, India

Keywords: Activated carbon, BET surface Area Capacitance, Carbon, Carbon nanosheets, Energy density, Flexible, Heteroatoms, Hierarchical pores, Human hair, Power density, Symmetric supercapacitor, Waste biomass, Redox active solid state electrolyte

ABSTRACT

This work reports a scalable method to synthesize hierarchically porous, hetero-atom doped activated carbon nanosheet from waste biomass—human hair, and demonstrates the use of this carbon as an ultrahigh performance electrode material for supercapacitor applications. Microscopic analyses reveal that sheet size ranges from 50 to 200 nm having a thickness of 15—27 nm. As-synthesized, carbon nanosheets possess a hierarchical porous structure having a specific surface area of 1548 $m^2 g^{-1}$. Heteroatom concentration (nitrogen,

oxygen, and sulfur) of around 25% is confirmed from XPS analysis. Therefore, the novel interconnected hierarchical porous nanosheets structure enables fast adsorption and transportation of ions during electrochemical processes. Also, the abundant chemically available electroactive heteroatom species in the material enhance the wettability of ions and contribute to pseudocapacitance. The electrochemical analyses through cyclic voltammetry and galvanostatic charge-discharge measurements in 6 M KOH reveal the quasi-EDLC behavior of the activated carbons due to the presence of heteroatoms. A reprensentative KOH activated carbon shows an excellent specific capacitance value of 999 Fg^{-1} at a current density of 1 A g^{-1}. The symmetrically assembled two-electrode device also delivers a maximum energy density of 32 W h Kg^{-1} at a power density of 325 W Kg^{-1} In addition, excellent cyclic stability of 98% capacitance retention is observed after 10,000 continuous GCD cycles even at a high current density of 5 A g^{-1}. Symmetric flexible supercapacitor device using KOH-PVA-K_3FeCN_6 as redox gel polymer electrolyte shows a synergistic specific capacitance of 145 mF cm^{-1} at a current density of 0.8 mA cm^{-1} exhibiting very less deviation in bending mode. Therefore, this waste biomass derived heteroatom doped hierarchical porous carbon nanosheets can be a promising material for cost-effective high- performance supercapacitor.

1. Introduction

Owing to the rise in environmental concern, significant efforts are being directed towards the study of biomass-derived commercially valuable materials. It acts as a material bank that can provide not only raw materials but also deliver great inspiration for humans to develop new materials with advanced structures [1]. Bioinspired design strategies give rise to unique nanostructured functional materials, which cannot be achieved via artificial synthesis. In this regard, carbon is the most abundant naturally occurring material in biomass which can be explored to a large extent due to its variant physicochemical properties. This enables its usage in a variety of applications [2,3]. Till now, a lot of research has been devoted to the extraction of functionalized carbon from naturally occurring biomasses [4—7]. Bio-wastes are useless products found in municipal waste streams in almost all cities and towns in the world. The bio-waste mainly contains hydrocarbons, which are cheaper to use and facile to produce activated carbon in large quantities. These include either a simple one-step or two-step carbonization and activation procedures [8,9]. The extraction of carbon from cheap biomass resources is providing a new path to develop carbonaceous materials, which can help in achieving high surface area, novel nanostructures, hierarchical porosity, and presence of heteroatoms/defects. Knowledge of underlying mechanisms and reactions can assist in obtaining these features by tailoring the synthesis process of carbon extraction from biomass, which has their own biological structures. These functionalized carbons find applications mainly as gas adsorbent [10], in catalysis [11], wastewater treatment [12], and as electrode material for energy storage systems [6,13,14].

For the supercapacitor application, it is directly used as an electrode for electric double-layer capacitor (EDLC), or it can form a composite with other materials to be utilized as a hybrid electrode material [15—19]. Biomass-derived carbon not only reduces the cost of carbon precursors, but the inherent biological structures and presence of heteroatoms (such as nitrogen, oxygen, and sulfur) provide excellent properties for electrode [5,6,20—32]. A variety of biomass precursors like kelp [5], corn [29], tremella [30], fish gill [33,34], and so on are used to prepare a three-dimensional porous network of carbon structure for supercapacitor electrode material [35,36].

In this vein, the human hair is widely available bio-waste predominantly made up of heteroatom-containing amino-acids [37]. This is one of the most abundant keratin waste, which slowly decomposes with time, eventually returning the constituents elements, namely carbon, sulfur, oxygen, and nitrogen to nature [38]. Due to slow degradation, it stays as lumps causing different types of pollution. The best way to address these problems is to utilize these waste material as a resource, which can also act as a helping hand towards waste management [37,39]. It is composed of tough protein, mainly keratin, which is a combination of amino acids like cysteine, serine, glutamic acid, etc. In elemental form, it contains 51% carbon, 17% nitrogen, 21% oxygen, 6% hydrogen, 5% sulfur, and a trace amount of Fe, Mg and other elements [37,38]. The presence of nitrogen-, oxygen-, and sulfur-containing species increases the wettability of activated carbon by acting as primary

sites for transportation or adsorption of ions and also contributes to the Faradaic capacitance [40]. Therefore, the activated carbon prepared from keratin of human hair has been studied for different applications such as electrochemical sensors [41], electrocatalysis [14], gas absorption [42,43], electrode material for solar cell [44], batteries [45], and supercapacitor [46—48]. The prepared activated carbon shows various structural characteristics when carbonized and activated in a different environment. Si et al. also studied the nitrogen and sulfur-doped carbon material through hydrothermal carbonization of human hair with glucose and subsequent activation with KOH for supercapacitor application. However, they achieved a specific capacitance value up to 264 F g^{-1} at a very low current density of 0.25 A g^{-1}, which decayed to 154 F g^{-1} just after 1000 cycles [48]. Qian et al. synthesized activated carbon flakes for the supercapacitor electrode through the carbonization of human hair fibers followed by activation using KOH. The obtained capacitance value for activated carbon derived from human hair was 340 Fg^{-1} at a current density of 1 A g^{-1}. However, they used toxic organic electrolyte to fabricate the supercapacitor device, which is detrimental to the environment [47]. A set of sample HHC3 and HHC3K2 (as named in this work) was prepared using similar synthesis condition [47]. Results obtained are similar to the reported literature [47]. The present work has been further carried out using a modified synthesis route. Great enhancement in terms of performance and morphology were obtained when carbonization and activation route was modified, which was also confirmed by detailed XPS and electrochemical studies.

Till now, low capacitance achieved by biomasses is limited due to its surface properties, and very small amount of heteroatoms participates in pseudocapacitance [5,47,49—51]. There is a need to tailor the choice of precursor, synthesis mechanism and temperature condition to prepare high performance activated carbon. Most of the carbon derived from the various biomasses uses simple carbonization and activation procedure. Again, most of the reports show micron level porous morphology. In this vein, an attempt is made to create nanoscale porous morphology. Herein, the present study reveals that the modification in the existing synthesis route can yield hierarchical porous interconnected heteroatom doped carbon nanosheets from waste keratin of human hair. During carbonization, waste human hairs are pyrolyzed till 900 °C for 1 h with a hold of 1.5 h at 220 °C. This step prevents the evaporation of volatile molecules and promotes the crosslinking of heteroatoms [52]. Also, the hold of 1.5 h provides enough time for heteroatoms to get rearranged in the carbon matrix of keratin of human hair. A similar procedure has been followed during KOH activation processes to prevent the loss of heteroatoms. Schematic representation of the modified synthesis mechanism is depicted in Fig. 1. The assynthesized KOH activated carbon nanosheets show i) porous features which ensure fast mass transportation, ii) large specific surface area promotes adsorption of ions, iii) abundant chemically available sites due to heteroatoms which facilitates electrochemical processes, iv) interconnected hierarchical pore structure, which promotes continuous electron transport pathway, and v) presence of nanosheets structure shortens ion diffusion paths [53,54]. Therefore, in three-electrode system, it delivers an excellent specific capacitance value of 999 F g^{-1} at a current density of 1 A g^{-1}. The symmetric two-electrode assembly shows high cyclic stability of 98%

up to 10,000 cycles at a high current density of 5 Ag^{-1} using 6 M KOH as an electrolyte. The symmetric supercapacitor devices are also delved into to show the potential practical utilization of the electrode materials using aqueous electrolyte for a supercapacitor device. The assembled symmetric supercapacitor derived from KOH activated carbon displays wide potential window of 1.3 V in aqueous electrolyte delivering an excellent energy density of 32 Wh Kg^{-1} at a power density of 325 W kg^{-1} and also maintains up to 214 W h Kg^{-1} even at a very high-power density of 8125 W kg^{-1} The achieved overall electrochemical performance is superior compared to other reported bio-mass derived activated carbons [50,53,55,56].

2. Experimental section

2.1. Materials

The waste human hair (HH) fibers were collected from barbershop at the campus of IIT Kanpur. Potassium hydroxide (KOH, Sigma Aldrich 99.99% purity), Zinc chloride ($ZnCl_2$, Thomas Baker), Phosphoric acid (H_3PO_4 Analytical Grade), Polyvinylidene fluoride (PVDF, Alfa Aesar), N,N-dimethylformamide (DMF, Qualigens Fine Chemicals, India), carbon black (Alfa Aesar), Potassium Ferricyanide (III) (K_3FeCN_6, Loba Chemie, India), Polyvinyl alcohol (PVA, Loba Chemie, India) were used in this experiment without any further purification. Deionized water was employed throughout the experiment for the treatment processes.

2.2. Preparation of keratin-derived functional carbon

Collected human hairs were thoroughly washed with deionized water and dried at 60 °C for 24 h. The dried hair fibers were cut into small fragments (~3—5 mm).

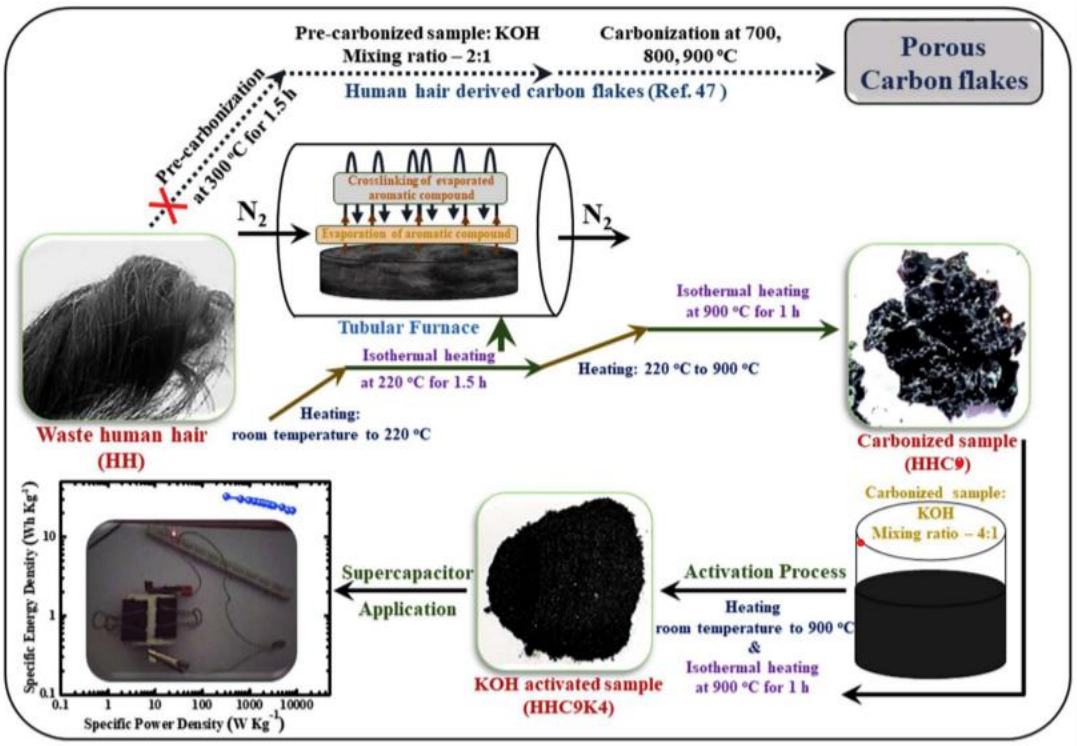

Fig. 1. Schematic representation for the preparation of activated carbons from keratin of human hair for supercapacitor applications

2.2.1. To study the effect of carbonization temperature

The hair fibers were carbonized in a horizontal furnace at 300 °C for 1h under N_2 atmosphere at the heating rate of 5 °C min^{-1}. The obtained carbonized sample was denoted as HHC3. Another set of human hair was pyrolyzed in a horizontal furnace at 220 °C for 1.5h and followed by carbonizing at 900 °C for 1 h under an N_2 atmosphere at the heating rate of 5 °C min^{-1}. The obtained sample was denoted as HHC9.

2.2.2. To study the effect of different activators

For the activation process, the carbonized human hair carbon (HHC9) sample was mixed with the activators (KOH, $ZnCl_2$, and H_3PO_4,) in the ratio of 4:1 in deionized water succeeded by drying the mixtures at 60 °C for 24 h. Dried mixtures were activated at 900 °C under N2 atmosphere for 1 h. Human hair derived activated carbon using different activators were denoted as HHC9K4, HHC9Z4, and HHC9P4 for KOH, $ZnCl_2$, and H3PO, activated samples, respectively.

2.2.3. To study the effect of impregnation ratio

The hair fibers carbonized at 300 °C (HHC3) and 900 °C (HHC9) were mixed with KOH in 2:1 and 4:1 ($weight_{KOH}$: $weight_{carbon}$) ratio and activated at 900 °C for 1 h at a heating rate of 5 °C min^{-1}. The obtained samples were denoted as HHC3K2 and HHC3K4 for HHC3

subjected to KOH activation in 2:1 and 4:1 impregnation ratio, respectively. For HHC9, activation at KOH impregnation in 2:1 and 4:1 ratio were denoted as HHC9K2 and HHC9K4, respectively. Here the samples were activated at 900 °C for 1 h with a hold of 1.5 h at 220 °C.

The obtained dark solid products were ground to powder and then washed thoroughly by deionized water. The KOH activated carbon samples were washed with 1 M HCI solution until neutral PH was achieved, followed by washing with deionized water. The residue was collected and dried at 60 °C in the oven. Fig. S1 shows the schematic process for human hair derived activated carbon via KOH activation at different temperatures.

3. Characterization

The microstructure and surface topography of the activated and non-activated human hair carbons were studied by using scanning electron microscopy (SEM; JEOL JSM-6010LA) and atomic force microscopy (AFM; Agilent 5500). The internal structure of the materials was further examined by transmission electron microscopy (TEM (HR-TEM), FEI Titan G2 60—300). Nitrogen sorption isotherm study was carried out using Quantachrome Instruments v3.01. The specific surface area and the pore size distribution were calculated using Brunauer—Emmett—Teller (BET) theory and Barrett-Joyner-Halenda (BJH) analysis, respectively. Raman spectra of the materials were analyzed by LabRam Micro Raman Spectrometer (Jobin-Yvon HR 800 UV) by using a He—Ne (632.81 nm) laser excitation source. X-ray diffraction (XRD) patterns were measured by PANalytical X'Pert for ultrafast X-ray diffraction on bulk and powder samples in the 28 range of 5—70° using Cu Ka radiation (wavelength of 1.5418 A) at a scan rate of 3° min^{-1}. X-ray Photoelectron Spectroscopy (XPS) (XPS; PHI 5000 Versa Probe II, FEI Inc.) was performed to analyze the chemical states of the elements present in the studied materials. The obtained peaks were analyzed using XPS peak version 4.1. Thermogravimetric analysis (TGA) was performed on a PerkinElmer Diamond thermogravimetric analyzer to study the thermal decomposition behavior of the HHs.

3.1. Electrochemical analyses

All the electrochemical analyses were carried out using Metrohm Autolab galvanostat/potentiostat electrochemical testing station at room temperature.

For the three-electrode system, the working electrode was prepared by mixing 80 wt% of the active material, 10 wt% of PVDF and 10 wt% of carbon black in 1 mL DMF solvent. The prepared solution was drop cast on nickel foam then pressed and kept in an oven at 60 °C for drying. Pt wire and Ag/AgCl were used as counter and reference electrodes, respectively. Cyclic voltammetry (CV) and galvanostatic charge-discharge (GCD) analyses were carried out in the potential range of 0 to —1.0 V versus Ag/AgCl electrode in 6 M KOH aqueous electrolyte.

3.2. Electrochemical analyses of symmetric supercapacitor

A symmetric two-electrode cell configuration setup was prepared by placing an equal amount of the active material in the two stainless steel plates, which act as a current collector. The two electrodes were separated by a filter paper soaked in 6 M KOH

electrolyte. The whole parts were integrated by teflon plate and tightly pressed by the paper clips to form a device. CV and GCD analyses were carried out in a potential range of O—1.3 V of the device. Electrochemical impedance spectroscopy (EIS) was measured in a frequency range of 0.1—10^5 Hz.

3.3. Electrochemical analyses of flexible supercapacitor

In order to study the application of electrode material for flexible and wearable electronics, a flexible supercapacitor was designed. HHC9K4 coated carbon fibers through electrophoretic deposition were used as an electrode material and KOH-PVA-K_3FeCN_6 was used as redox-gel polymer electrolyte [57,58]. The assembled device was integrated tightly using Teflon tape. The CV and GCD analyses were carried out in a potential range of O—1 V of the device in both bending and straight mode. The specific capacitance value was calculated using equation S(8).

4. Results & discussion

4.1. Synthesis activated carbon from hierarchically structured keratin in human hair

Human hair is a low cost and abundant bio-based waste material. Around 51% of carbon is present in elemental form, making it a very rich source of carbon. Human hair shows a lamellar scale-like structure containing an abundance of N, O, and small amounts of S moieties. Pyrolysis of human hair results in the synthesis of N-, O-, and S-containing functionalities into the carbon matrix [59]. The thermal behavior during heat treatment of human hair was studied through a TGA thermogram to determine the pyrolysis profile before the carbonization of human hair, which is shown in Fig. S2. The thermogram reveals that initial weight loss below 90 °C is due to the removal of moisture and other volatile impurities. The temperature derivative of weight loss (dW/dT) shows that human hair decomposes in two major steps. The major degradation step occurs between 170 and 300 °C, where the evolution of inorganic gases occurs [60]. The evolution of gases promotes physical activation and subsequent doping of heteroatom species into carbon skeleton [61]. During human hair carbonization at 900 °C, the aim of holding human hair at 220 °C for 1.5 h is to increase the crosslinking of the inorganic compound with carbon atom followed by rearrangement of carbon structure by continuing pyrolysis at high temperature (900 °C) [52]. Activators H_3PO_4, and $ZnCl_2$ show dehydration effect during activation on carbon char, which promotes crosslinking reaction inside the carbon matrix. This reduces the carbon

particle dimension, hence porosity decreases [62]. Also, activation in the presence of KOH increases porosity due to the oxidation process which remove some carbon atom [46]. The activation temperature of 900 °C was maintained for 1 h to ensure the complete removal of volatile compounds. Also, another set of samples are prepared for comparison via carbonization at 300 °C and subsequent KOH activation at 900 °C [47]. Fig. S2 shows that at temperature 300 °C major initial weight loss of human hair takes place. The motivation to choose a carbonization temperature of 300 °C is to study the effect of incomplete carbonization followed by its KOH activation at 900 °C. The comparative structural and elemental studies (discussed in section 4.2) show that samples HHC3K2 and HHC3K4 reveal a porous structure with fewer heteroatoms. Whereas for HHC9K2 and HHC9K4, the isothermal treatment at 220 °C during carbonization promotes crosslinking of volatile/inorganic species with carbon matrix, and a further increase in temperature increases aromatization and concentration of heteroatoms. The nomenclature of the sample is given in Table 1.

4.2. Material characterization of activated carbon

The morphology of the prepared activated carbon is characterized by SEM analysis. Fig. S3 shows the SEM micrographs of nonactivated carbonized human hair and chemically activated carbonized human hair. Figs. S3a and b show the SEM micrograph of HHC3 and HHCY, which reveals the formation of carbon blocks with rough surface contributing to minimal porosity after the carbonization of human hair at 300 and 900 °C, respectively. Figs. S3c and d show that after activation of the HHC9 with H_3P0_4, and $ZnCl_2$, respectively the structure of the carbon blocks remains unchanged with non-porous fragments, despite of the hightemperature activation (900 °C) whereas, all KOH activated samples form porous morphologies. Also, the variation in the impregnation ratio results in different morphologies [62]. Figs. S3e—g shows the SEM micrograph of HHC9K2, HHC3K2, and HHC3K4, respectively results in interconnected porous morphology. SEM micrographs clearly indicate the porous structure although, pore size varies with the sample, which indicates the influence of impregnation ratio and carbonization temperature. The result shows that KOH activation leads to the development of pores via metallic intercalation and gasification of released gases [63].

Fig. 2a shows the SEM micrograph of HHC9K4 which reveals interconnected highly porous sheet-like structure where the sheets were assembled to form beads of 50 to 200 nm in diameters. The thickness of carbon nanosheets is quantified using AFM in Fig. 2b, which shows a highly interconnected structure having a sheet thickness of 15—27 nm. The height profile of nanosheets is shown in Fig. 2c. Also, nanosheets overlap together and are interconnected to form a channelized carbon structure, which provides efficient ion transportation. Fig. S4a shows the 3-D AFM images along with the height profile curve (Fig. S4b). Carbon nanosheets with interconnected two-dimensional morphology possess an_ intrinsic advantage over planar morphology such as graphene. The porous features of nanosheets provide efficient mass transportation and provide sites for electron adsorption.

The presence of interconnected hierarchical porous structure reduces the ion transport length and allows non-resistive transportation of electron [50,54,64]. It can be observed that the nature of activators, impregnation ratio, and carbonization temperature play an important role in determining the properties of activated carbon. The modified synthesis mechanism provides a more convenient and common strategy to prepare porous carbon nanosheets via biomass, whereas simple carbonization and activation leads to three-dimensional porous morphology.

The detailed morphological characteristics of HH derived KOH activated carbon are studied through HR-TEM analysis. TEM and HR-TEM morphology of HHC3 in Figs. S5a and d and HHC9 in Figs. S5g and j, respectively. Significant content of the heteroatom substituted ordered phase of carbon precursor having an interplanar spacing of 0.25 nm corresponding to (002) graphitic plane is observed for HHC9. Whereas for HHC3, connected carbon blocks containing other inorganic molecules are observed with no presence of graphitic phase. This is attributed to the incomplete carbonization of human hair for HHC3. The TEM micrographs of HHC3K2 (Figs. S5b and e) and HHC3K4 (Figs. S5c and f) show the presence of the huge amount of pores, which offer a large number of electrolytic ions to get adsorbed at the surface. Figs. Ssh and k show the TEM and HRTEM images of HHC9K2 where along with the high concentration of porous structure, a small amount of graphite-like phase is observed. At higher impregnation ratio, i.e. for HHC9K4, HR-TEM micrograph in Fig. 2d shows layered nanosheet type morphology of activated carbon which are surrounded by a large amount of co-connected mesoporous morphology having pore diameter ranging from 3 to 5 nm. Fig. 2e shows a plenty of graphitic phases having interplanar spacing 0.34 nm. The presence of porous structure is further confirmed with nitrogen adsorption and desorption studies, which is discussed in the following section. The well-dispersed graphitic pockets induce the enhancement in conductivity of ions inside the sample and the presence of porosity provides sufficient sites for electrolytic ions to get penetrated. More clear TEM images of HHC9K4 particles are provided in Figs. S5i and |. The above study concludes that the carbonization at a high temperature of 900 °C leads to the formation of a graphitic phase, which increases the conductivity of KOH activated samples, hence efficient charge transportation.

Table 1

Nomenclature of samples

S. No.	Sample synthesis process	Sample Nomenclature
1	Human hair	HH
2	Sample carbonized at 300 °C	HHC3
3	Sample carbonized at 300 °C followed by KOH impregnation in 2:1 ratio and activation at 900 °C	HHC3K2
4	Sample carbonized at 300 °C followed by KOH impregnation in 4:1 ratio and activation at 900 °C	HHC3K4
5	Sample carbonized at 900 °C	HHC9
6	Sample carbonized at 900 °C followed by KOH impregnation	HHC9K2

	in 2:1 ratio and activation at 900 °C	
7	Sample carbonized at 900 °C followed by KOH impregnation in 4:1 ratio and activation at 900 °C	HHC9K4
8	Sample carbonized at 900 °C followed by ZnClz impregnation in 4:1 ratio and activation at 900 °C	HHC9Z4
9	Sample carbonized at 900 °C followed by H3PO, impregnation in 4:1 ratio and activation at 900 °C	HHC9P4

The porosity measurement of HHC9K4 is carried through nitrogen adsorption-desorption isotherm, as shown in Fig. 3a. According to IUPAC classification, HHC9K4 exhibits a mixture of type-I and type-IV isotherms [6,63]. The dominance of type-I isotherm is obtained, which is the characteristics of microporous materials. The rapid uptake at very low pressure signifies the presence of ultramicropores in small concentrations. Also, at high relative pressure, type-IV isotherm behavior is observed, which is due to capillary condensation in mesopores [6]. The BET surface area of HHC9K4 is 1548 $m^2 g^{-1}$. Fig. 3b shows the pore size distribution, where BJH pore volume is 0.063 cc g^{-1}. The whole isotherm of HHC9K4 signifies the dominance of mesopores, with the highest volume of diameter 3 and 5 nm. The obtained hierarchical porous structure is due to the decomposition of potassium salts which induces gasification effect by the following reactions [22,36,63]:

$6KOH + 2C > 2K + 3H_2 + 2K_2>CO_3$ (1)

K_2CO_3 — $K_20 + CO_2$ (2)

Hierarchical pore structure plays an important role in the determination of electrode properties. Macropores have large pore diameters (>50 nm) possess a small surface area. Macropores act as ion reservoirs of electrolytic ions, to provide sufficient ion source for the adsorption of electrolytic ions on the surface of meso- and micropores. The presence of mesopores (pore diameter 2—50 nm) improves the accessibility of electrolytic ions by providing a resistance-free transfer pathway for the migration and fast diffusion of electrolyte ions. Micropores, on the other hand, provide additional capacitance by providing a large amount of ion adsorption sites for the formation of an electric double layer. Thus, different pores have a different function that collectively increases the electrode performance. Proper pore size distribution is of utmost important property for high capacitance and excellent rate capability electrode material [65,66]. Prior report obtained a BET surface area of 669 $m^2 g^{-1}$ with pore volume 0.45 $cm^3 g^{-1}$ for HHC3K2 [47]. The sample indicates the enhancement in the surface area via activation with the formation of mesopores and macropores. Fig. S6a shows the BET sorption curve of HHC9, HHC9Z4 and HHC9P4. Table S1 depict the porous properties of HHC9, HHC9Z4 and HHC9P4, where no significant enhancement is observed after $ZnCl_2$ and H_3PO_4, activation.

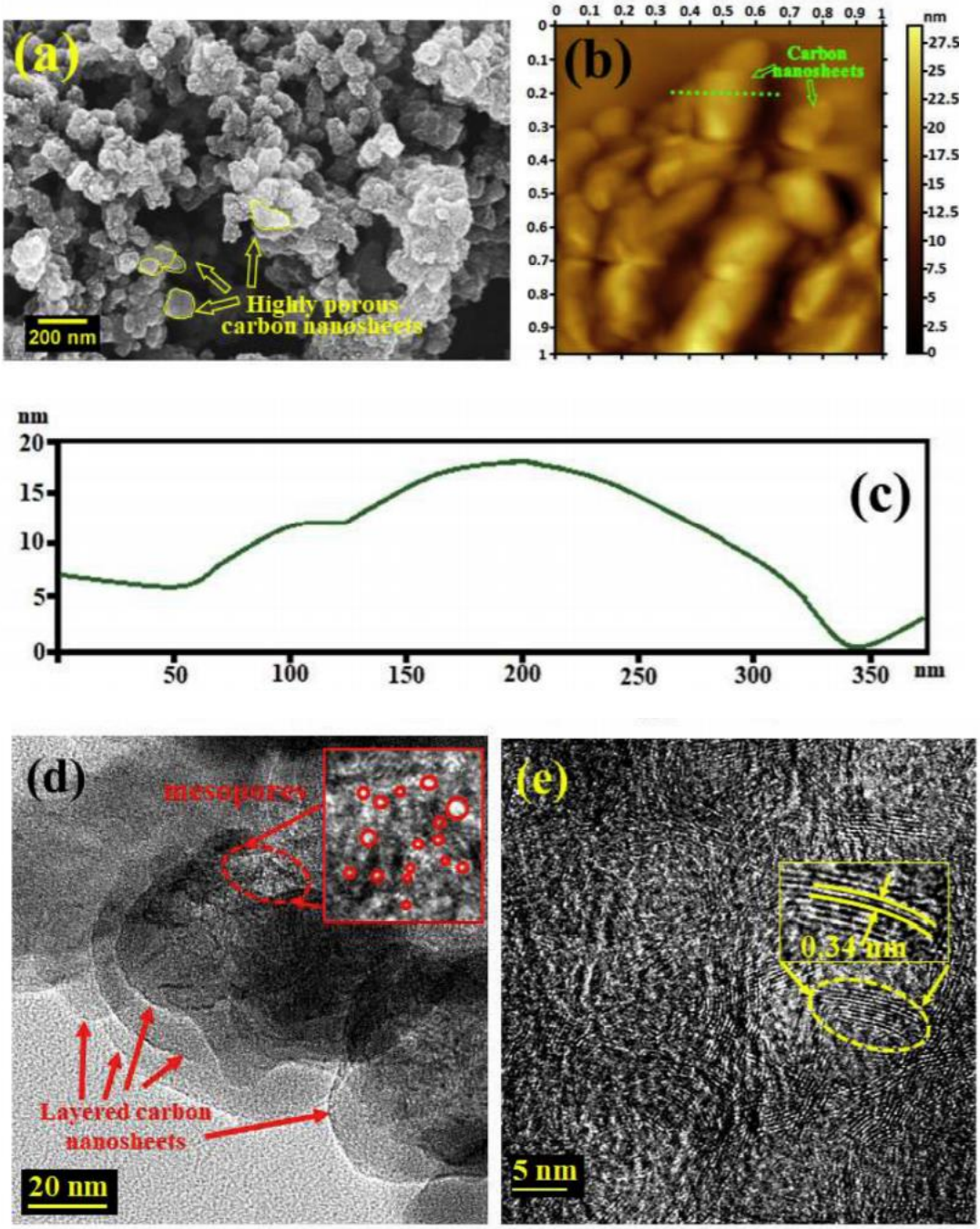

Fig. 2. (a) SEM micrograph, (b) AFM height-deflection profile, (c) Height-distance line profile, HR-TEM micrograph of HHC9K4 showing (d) well defined layered carbon nanosheets structure, the white spot inside the red circle representing pore with diameter of 2 and 5 nm and (e) well defined graphitic fringes with a distinct interplanar spacing of 0.34 nm.

Raman spectroscopy is extensively used to characterize carbon materials, as they are sensitive towards minute changes in structure. So, the structures of the as-synthesized carbons were further characterized by Raman analysis. Fig. 3c shows the Raman spectra of the HHC3, HHC9 and KOH activated carbons. However, partially carbonized HHC3 sample

contains inorganic species (heteroatom functionalized diluted carbon) and, therefore, it shows inherently weak Raman signal. Raman spectra for H_3PO_4 and $ZnCl_2$ activated samples are shown in Fig. S6b. Two distinguished peaks mainly attributed to D-band (disorder and defect) and G-band (graphitic) are observed. G peak corresponds to the inamsiion, of doubly degenerate species E_{2g}, due to C— C stretching with sp^2 hybridization. D peak corresponds to sp^3 hybridization with A_{1g} symmetry [67]. The high-intensity ratio of D and G peak (I_D/I_G) shows that the degree of disorder is high resulting in the shift from sp^2 to sp^3 hybridization of carbon atoms. Here, the I_D/I_G ratio for HHC9, HHC9K2 and HHC9K4 are found to be 1.25, 1.23 and 1.14, respectively. The decrease in the ratio indicates the formation of graphitic phases, which goes well in accordance with HR-TEM results. Whereas, I_D/I_G ratio for HHC3K2 and HHC3K4 are 1.17 and 1.27, respectively which show the opposite trend with respect to HHC9 set of samples. Also, it is well known that the degree of graphitization is inversely proportional to the distance between the defects (L_a) which can be calculated by equation (3). It measures the interdefect nanocrystallite size [52].

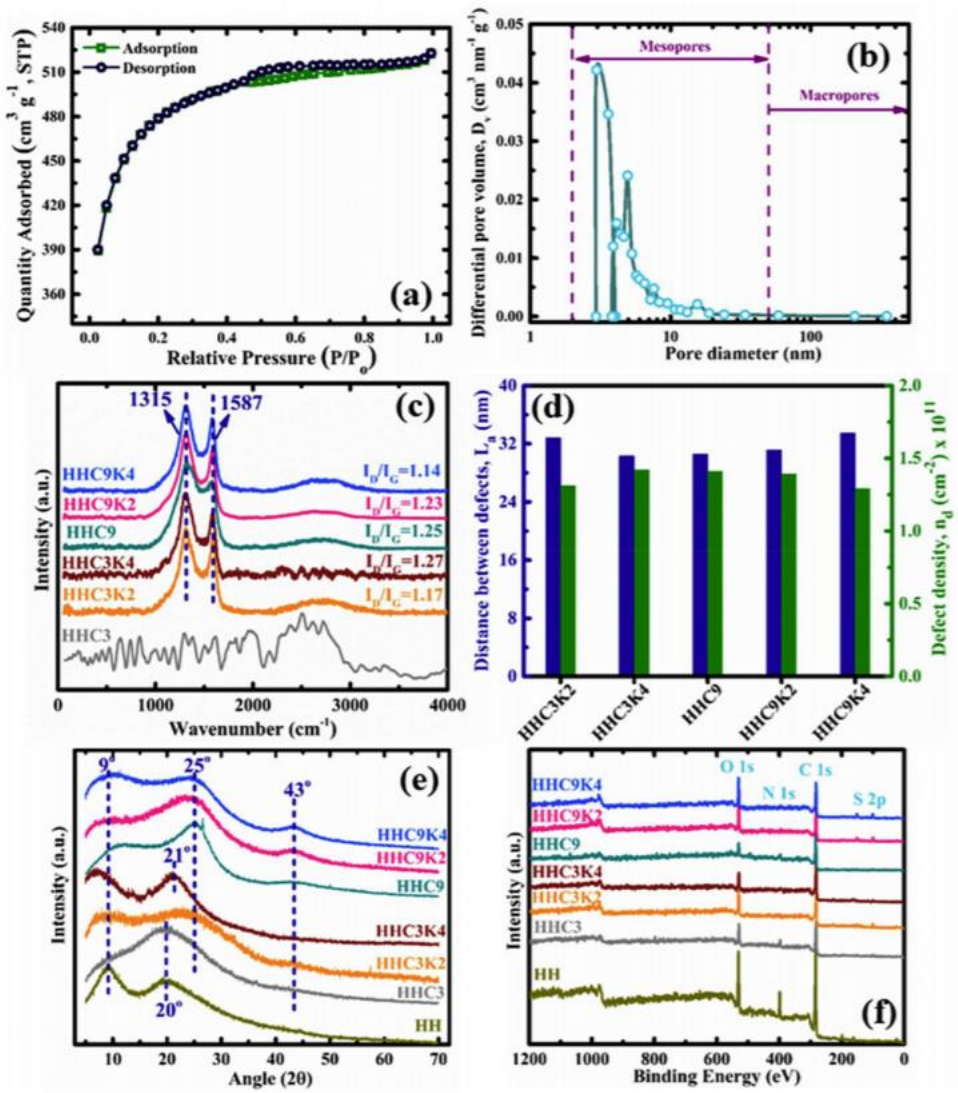

Fig. 3. (a) Nitrogen adsorption-desorption isotherm, (b) BJH pore size distribution profile of the HHC9K4 depicting the dominance of mesopores with two maxima at 3 and 5 nm, (c) Raman spectra, (d) Variations of the distance between defects (L_d) and defects density (n_d), (e) XRD patterns and (f) XPS spectra, of the carbonized and KOH activated samples.

$$L_d(\text{nm}) = (2.4 \times 10^{-10}) \times \lambda^4 \left(\frac{I_D}{I_G}\right)^{-1} \quad (3)$$

Similarly, defect density (ng) can be determined by equation (4) [52].

$$n_d(\text{cm}^{-2}) = \frac{(1.8\pm \times 10^{22})}{\lambda^4} \times \left(\frac{I_D}{I_G}\right) \quad (4)$$

Where, λ is the excitation wavelength and I_D/I_G is the intensity ratio corresponding to D and G bands, respectively. Fig. 3d shows that the interdefect distance increases and defect density decreases from HHC9 to HHC9K2 to HHC9K4. This indicates the increase in graphitic order due to more exfoliation of carbon structure by KOH and thermal treatment as well as by heteroatom doping (N, O, and S) [47]. Whereas, on increasing the KOH impregnation ratio for 300 °C carbonized sample, defect density increases which indicates more disorders. It happens because of the decomposition of a large amount of carbonaceous species around heteroatoms. Most of the inorganic species are not eliminated during carbonization at 300 °C but, during KOH activation at 900 °C these inorganic species get eliminated giving rise to porous structures. Therefore, these results are in good agreement with the microscopic analyses.

Fig. 3e shows the XRD pattern of a human hair (HH), carbonized and KOH activated samples. Fig. S6c shows the XRD pattern of H_3PO_4 and $ZnCl_2$ activated samples. The two diffraction peaks appeared at 20 is 9° and 20° of HH correspond to α-helix structure and β-sheet crystalline structure of keratin, respectively [68,69]. The crystalline degree of human hair decreases significantly after pyrolysis treatment due to the decomposition of inorganic molecules followed by further activation. The two diffraction peaks located at 25° correspond to (002) planes and 43° correspond to (100) planes of graphite after carbonization of HH. In HHC3 derived sample, peak at ~20° due to incomplete degradation of keratin structure. The other peak in the range of 20° to 25° shows the restacking of graphitic layers. The broad hump at 9° indicates the existence of layered structure which might be due to the exfoliation of carbon layers by KOH and thermal treatment [70]. This results in randomly arranged carbon sheets that are not stacked in parallel showing disordered turbostratic porous carbon structure [59]. HHC3K2 possesses micron level porosity along with intrinsic defects and disordered structure as depicted in SEM micrograph (inset: Fig. S3f). On the other hand, HHC3K4 shows minimal porosity with rough surfaces. The sharp peak at 21° for HHC3K4 indicates near crystalline carbon monolith structure. This peak gets to shift and broaden for HHC3K2 due to a large amount of porous surface even at bulk carbon blocks (produced via effective activation), depicting the presence of a much higher degree of amorphous nature than HHC3K4.

The elemental composition, chemical states, and doping of N, O, and S in the activated carbon are further analyzed by XPS. Fig. 3f shows the full scan of the human hair, carbonized and KOH activated samples. Fig. S6d shows a full scan of H_3PO_4 and $ZnCl_2$ activated samples. All the samples reveal the presence of C, O, N, and S elements indicating successful incorporation of heteroatoms doped activated carbon. The main classes of heteroatom-containing compounds are nitriles, pyrroles, pyridines, amides, sulfides, thiols, thiazoles, and thiophenes. These functionalities originate from the initial amino acids in the composition of keratin [60,68]. This shows the advantage of using biowaste as a carbon precursor that provides effective inherent incorporation of heteroatom species, which otherwise are incorporated externally via hazardous chemical reaction using energy-intensive processes. The amount of these elements (in atomic %) in the materials is shown in Table 2. At an activation temperature of 900 °C, the activation occurs due to the presence of KOH. KOH activation alters the morphology, porosity, and surface area of the sample. Almost half the amount of KOH has been used in the activation process for HHC9K2 as compared to HHC9K4. Since, the KOH activator amount is less in HHC9K2, during isothermal treatment at 900 °C for 1 h, a small fraction of heteroatom may come out and get eliminated from the carbon matrix. Simply, in absence of adequate KOH other heteroatoms play a role in activating the carbon. In contrast we find when abundant KOH is available heteroatoms are retained. The radius of the sulfur atom is 100 p.m. which is much higher than carbon atom having an atomic radius of 70 p.m. and other heteroatoms (nitrogen: 65 p.m. and oxygen 60 p.m.). So, sulfur atoms became most likely heteroatom to get eliminated from the carbon surface during the high-temperature isothermal hold for HHC9K2. It can be clearly seen that HHC3 and HHC9 show nearly equal amounts of heteroatom species (HHC9: 21.31% and HHC3: 25.6%). Also, samples activated from HHC9 shows an increment of about 4.2% (for KOH impregnation 2:1) and 7.9% (for KOH impregnation 4:1) compared to that of sample activated from HHC3. This shows that isothermal hold of 1.5 h at 220 °C for HHC9 prevents the loss of inorganic species and incorporate them into carbon skeleton.

Table 2

Atomic percentage of the elements determined by XPS analysis of human hair, carbonized and activated samples.

Sample	C	O	N	S
HH	69.30	18.70	11.30	0.60
HHC9	78.69	10.93	9.26	1.12
HHC9K2	76.63	21.06	2.31	0.00
HHC9K4	75.23	21.15	3.16	0.47
HHC3	74.40	14.44	10.06	1.10
HHC3K2	80.83	17.04	2.00	0.12
HHC3K4	83.10	12.89	2.73	1.28
HHC9P4	77.00	17.70	5.30	<1
HHC9Z4	77.80	16.30	5.80	<1

Figs. 4,S7 and S8 show the binding states of C1s,O 1s,N1sandS 2p for all samples. Deconvolution of C 1s spectra (as shown in Figs. 4a, S7a and S8a) show peaks at 284.1—284.6 eV corresponding to sp^2 hybridized carbon in aromatic environment. Other peaks at 285.1—285.5 eV corresponds to the carbon atom bonded with nitrogen, oxygen and sulfur atom having functionalities such as pyrrolidonic, phenol, ether, thioether and thiophene. The peak at 286.3—286.8 eV reveals the presence of sp^3 hybridized carbon. Peaks at 287.2—287.8 eV and 290.4—291 eV correspond to carbonyl, ester and carboxylic group, respectively [37,48]. Four distinguished peaks at 397.7—398.5, 399.9—400.1, 401—402 and 403.3 eV are observed after deconvolution of the N 1s spectrum of human hair precursor (Figs. 4b, S7b and S8b). HH shows pyridone groups at 399.5 eV due to the presence of proteins in human hair [71]. Carbonized and activated samples show four different nitrogen binding states corresponding to pyridinic N (397.7—398.5), pyrrolic N (399.9—400.1 eV), graphitic N (401—402), and Pyridinic-N-oxide (403.3 eV) [13,71]. Pyridinic N represents the nitrogen atom bonded with two carbon atoms in six-membered rings. Pyrrolic N represents nitrogen in a five-membered ring neighbor of the carbon atom. Graphitic N represents nitrogen atom bonded with three carbon atoms centrally which enhances the conductivity of carbon skeleton. The presence of pyrrolic, pyridinic, and pyridinic N-oxide functional groups enhances the energy storage performance by providing pseudocapacitive reactive sites [72,73]. Deconvoluted O 1s spectra (as shown in Figs. 4c, S7c and S8c) of activated carbon show three types of bonding structure at 530.9—531 eV corresponding to carbonyl (C=O) and/or quinone, 532—532.5 eV to the hydroxyl (C—OH) and ether (O—C—O) groups, 532.7—533.1 eV corresponds to carboxyl ($O=C—O^-$) and 534.4 eV to amide bonds [48,73]. The presence of oxygen functional groups like carbonyl, quinone, hydroxyl, and ether undergo electrochemical redox reactions which enhance the pseudocapacitance. Further, after deconvolution of S 2p spectra (shown in Figs. 4d, S7d and S8d), peaks at 163.5—163.9 eV and 164.5—164.7 eV corresponds to the thiophenic group and peak at 167.9 eV and 169.3 eV corresponds to oxidized sulfur species [37]. The variable oxidation state of sulfur species enables the accumulation of electrons at the electrode. Table S2 shows a summary of the peak assignment of different heteroatom functionalities. The comparative study of HHC9K4 with different biomass-derived activated carbon (as shown in Table 3) shows that nanosheet morphology with a large amount of mesopores provides an effective surface area for ions to get adsorbed at the surface. An increase in the degree of graphitization confirms the presence of graphitic phases. Also, an extremely high amount of heteroatoms improves the conductivity and participate in pseudocapacitance during the charge-discharge mechanism.

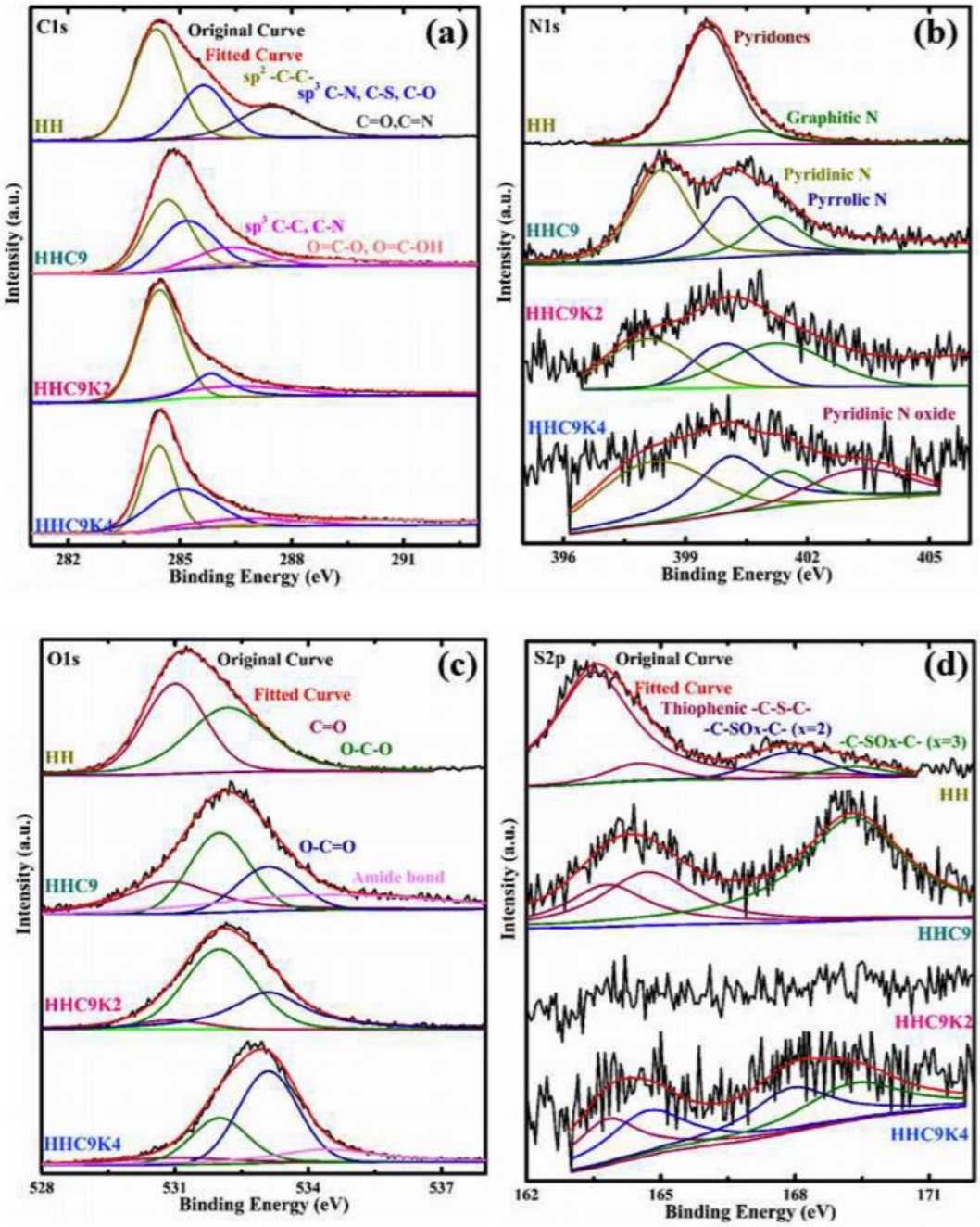

Fig. 4. Deconvolution of XPS spectra of the HH, HHC9, HHC9K2 and HHC9K4 for (a) C 1s, (b) N 1s, (c) O 1s and (d) S 2p

4.3. Electrochemical performance

The electrochemical performance of the activated carbons is evaluated using 3 electrode setup in 6 M KOH electrolyte at room temperature through performing CV and GCD analyses. The activated carbon materials are used as the working electrodes, Pt wire acts as

a counter electrode and Ag/AgCl acts as a reference electrode. The CV measurement is performed in the potential range of 0 to —1.0 V to obtain the best performance of the electrode material. Fig. S9a shows the comparative CV curves at a scan rate of 50 mVs^{-1} of the HHC9, HHC9P4, HHC9Z4, and HHC9K4. The curve indicates that HHC9K4 shows the highest enclosed area whereas, no significant improvement in H_3PO_4 and $ZnCl_2$ activated samples were observed as compared to the carbonized sample (HHC9). This indicates that high activation temperature of HHC9P4 and HHC9Z4 results in pore shrinkage, as H_3PO_4 and $ZnCl_2$ act as dehydrating agent [79]. In contrary to this, KOH is an oxidizing agent, which helps to develop ordered pore structure delivering excellent supercapacitive properties over other activators in GCD (Fig. S9b), EIS (Fig. S9c), and rate capability (Fig. S9d). This is due to the successful activation by KOH, whereas H_3PO_4 and $ZnCl_2$ lead to nonporous fragments of the carbon blocks. The result shows well agreement with SEM analysis (see Figs. S3c and d).

Table 3

Comparative material properties of different biomass-derived activated carbons with the present work.

Biomass	Morphology	BET SSA (m^2g^{-1})	V_t(cm^3g^{-1})	I_D/I_G	XPS				Study	Ref. No.
					C	N	O	S		
Human hair(HHC9K4)	Hierarchical porous heteratom doped carbon nanosheets	1548	0.063	1.14	75.23	3.16	21.15	0.47	-Study of carbonization temperature variation -Study of impregnation ratio variation	Present work
Crab shell	Porous structure	1656	–	0.99	87.62	1.68	10.7	–	Study of activation temperature variation	[74]
Natural bark	Carbon nanosheet	2159	0.96	1.2	92.26	1.87	5.87	–	Study of activation temperature variation	[75]
Soya	Interconnected porous surfaces	1072	0.455	0.83	84	5.3	10.7	–	Study of activation temperature variation	[13]
Platanus fruit	Micro carbon fibers	2015	1.09	0.72	92.29	1.23	6.35	0.13	Study of activation temperature variation	[24]
Algae	Sponge-like 3D interconnected carbons.	1879	0.99	0.44	87.35	0.85	11.8	–	Study of activator concentration variation	[76]
hemp	Interconnected partially graphitic carbon nanosheets	2287	1.45	0.85	93.39	1.01	5.6	–	Study of activation temperature variation	[50]
Bamboo-based industrial by-product	Beehive-like hierarchical nanoporous carbon	1472	0.61	1.01	94.56	4.79	0.65	–	Study of hydrothermal and pyrolysis synthesis mechanism	[77]
Auricularia	Layered porous structure	1607	1.51	1.02	88.4	4.8	6.8	–	Study of carbonized and activated samples	[78]
Silk	Hierarchical porous nitrogen-doped carbon nanosheets	2494	2.28	1.15	91.8	4.1	4.1	–	Study of carbonized and activated samples	[53]
Kelp	Porous carbon piles showing 3D architecture	1002.6	0.62	1.07	86.2	5.04	8.76	–	Study of carbonzation process in different gases (NH_3 and Ar)	[5]
Human hair	Carbon fakes	1306	0.9	1.23	88.72	4.38	5.39	1.51	Study of activation temperature variation	[47]
Celtuce Leaves	distorted layered microstructure	3404	1.88	–	95.69	3.75	0.56	–	Study of carbonization and activation	[35]
Corn cob	Cheese-like mor-phology with abundant pores	3475	1.8	1.01	91.23	–	8.77	–	Study of activation temperature variation	[29]
Cow dung	Porous morphology	1984	0.91	–	–	–	–	–	Study of activator concentration variation	[49]

Among different activators, KOH based activated carbon shows superior performance. So, the study has been further carried out by preparing KOH activated carbon using different carbonization temperatures and the KOH impregnation ratio. Fig. 5a shows the CV curves of carbonized (300 °C and 900 °C) and KOH activated samples at a scan rate of 50 mV s^{-1}. HHC3 and HHC9 show minimal enclosed area due to less interaction of electrolytic ions. This is because the thermal treatment of human hair leads to the formation of carbon blocks, which lack functionalities and porosity. The CV curves of HHC3K2 and HHC9K2

exhibit nearly symmetric rectangular voltammograms, indicating excellent electric double layer capacitor behavior. The CV curves of HHC3K2 and HHC9K2 at different scan rates are shown in Figs. S10a and b, respectively. The large area enclosed in CV curve shows that the charges are stored by the accumulation of a large amount of electrolytic ions at the electrode surface due to a 3D hierarchical porous structure, as seen in the SEM micrograph (Figs. S3e and f). HHC3K4 show small enclosed area, which indicates a low surface area of the electrode for the accessibility of the electrolytic ions. This may be due to excessive etching of HHC3 by KOH at high temperatures, which results in the evolution of a large amount of inorganic species and decreases the porosity of carbon. The quasi-rectangular behavior and large enclosed area of CV curve for HHC9K4, infer the contribution of pseudocapacitance along with double layer behavior. The deviation from ideal rectangular behavior is due to the presence of a large amount of heteroatoms (~25%). The large enclosed area of CV indicates that a huge amount of electrolytic ions get adsorbed at the electrode surface, due to high surface area and hierarchical pore size distribution as confirmed with sorption isotherm study. Even at a high scan rate 300 mV s^{-1} (shown in Fig. 5b), HHC9K4 maintained quasi rectangular shape, inferring fast kinetics of electric double layer formation, low internal resistance, and good rate capability. The well balanced hierarchical porous structure provides good rate capability at a high scan rate. The electrochemical performance of the materials is further analyzed by GCD as shown in Fig. 5c, where HHC3K2 and HHC9K2 depict symmetric and linear curve, which is a typical characteristic of ideal double-layer capacitor behavior. These GCD results further consolidates the observations of CV measurements. The capacitance value obtained for HHC3K2 is 328 F $g^{-1}$and HHC9K2 is 471 F g^{-1}|, at a current density of 1 Ag^{-1} as calculated from the Equation S1. The capacitance value achieved is comparable to the reported literature for human hair as biomass carbon precursor [46,48]. GCD at different current densities for HHC3K2 and HHC9K2 are shown in Figs. S10c and d, respectively. Further, the GCD curve of HHC9K4 shows linear and symmetric behavior with slight distortion around —0.2 to O V. It exhibits the highest specific capacitance value of 999 F g^{-1} at a current density of 1 A g^{-1} as calculated from the Equation S1. The extremely high capacitance is due to interconnected hierarchical porous nanosheets structure, where small pores enhance the adsorption and transportation of ions and large pores facilitate penetration of electrolyte ions and fast charge accommodation. Also, the literature suggests that heteroatoms take part in different Faradaic reactions during electrochemical analysis, which enhance the specific capacitance value [80—82]. The possible reactions of the heteroatoms in the presence of KOH are as follows:

Nitrogen atoms are mainly present in binding states of pyridinic N, pyrrolic N and graphitic N. The literature suggests that the graphitic N improves the electron transfer mechanism whereas pyridinic N and pyrrolic N enhance the pseudocapacitance by possible Faradaic reactions [80],

Pyrrolic N: $>C{=}NH_2 + 2OH^- \leftrightarrow >C{=}NH + 2e^- + H_2O$

Pyridinic N: $>C{-}NH_2 + 2OH^- \leftrightarrow >C{-}NHOH + 2e^- + H_2O$

Oxygen atoms are mainly present in binding states of carbonyl, hydroxyl, and carboxyl functional groups. These groups enhance pseudocapacitance by possible Faradaic reactions [80],

Hydroxyl: $>C{-}OH + OH^- \leftrightarrow >CO^- + H_2O$

Carbonyl: $>C{=}O + OH^- \leftrightarrow -COOH + e^-$

Carboxyl: $-COOH + OH^- \leftrightarrow -COO^- + H_2O$

Whereas, sulfur atoms are present in the form of thiol (>S) and sulfite (SO%) groups. The possible redox reactions may be as follows [81],

Thiol > $SH + OH^- \leftrightarrow >S{-}OH$

Sulphite > $S{-}OH + OH^- \leftrightarrow -SO_3H$

These re-oxidized groups function as electron shuttles during electrochemical analysis [82].

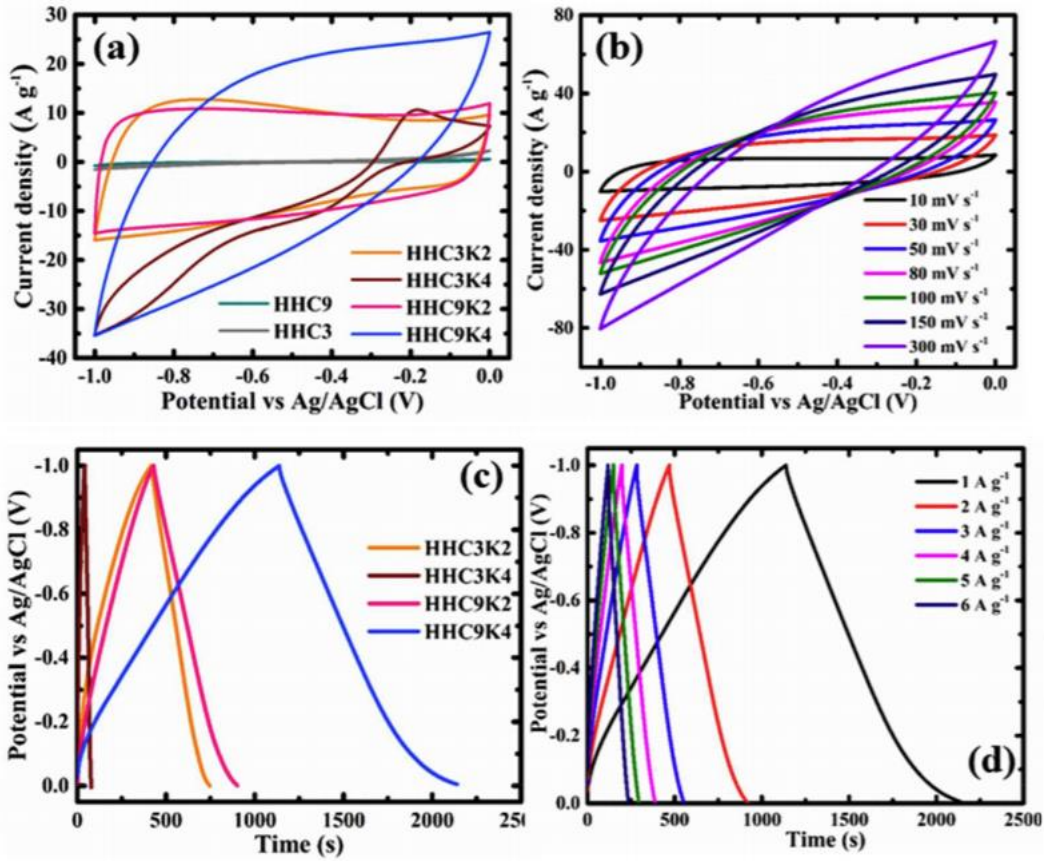

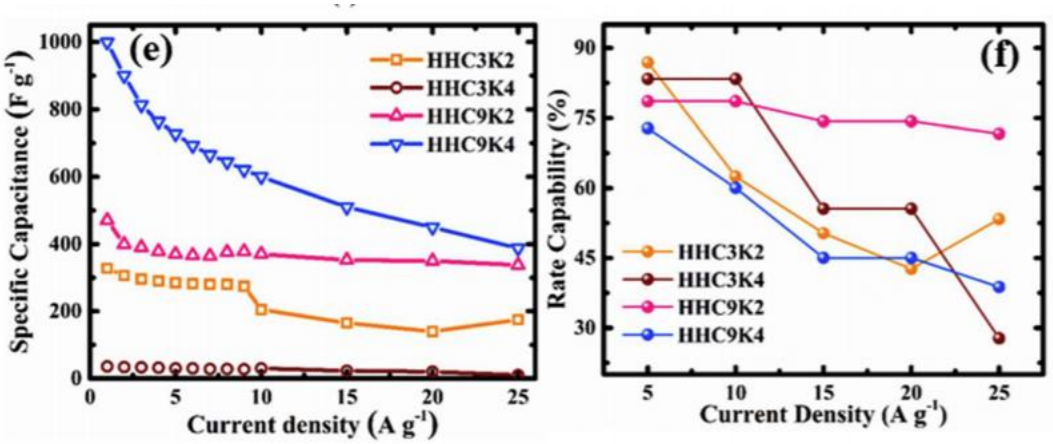

Fig. 5. Electrochemical performance of the human hair derived KOH activated carbons using 3 electrode system: (a) CV curves of carbonized and KOH activated samples at scan rate 50 mV s^{-1}, (b) CV curves of HHC9K4 at different scan rates, (c) GCD curves at 1 A g^{-1} current density for HHC3K2, HHC3K4, HHC9K2 and HHC9K4, (d) GCD curves of HHC9K4 at different current densities (e) Specific capacitance of HHC3K2, HHC3K4, HHC9K2 and HHC9K4 at different current densities, and (f) Rate capability vs. current density plot for HHC3K2, HHC3K4, HHC9K2, and HHC9K4.

Fig. 5d shows GCD curves of the HHC9K4 sample at different current densities, where charge-discharge time decreases as the current density increases. The small deviation of linearity in potential-time GCD curves is attributed to the redox reactions of the heteroatoms present in the structure [25]. The comparative specific capacitance values of the studied KOH activated carbon at different current densities are shown in Fig. 5e. For better understanding, Fig. 5f shows the graph between the rate capability of KOH activated samples over different current densities. The graph shows that at a high current density of 10 A g^{-1}, HHC9K4 shows 60%, HHC9K2 shows 78.5%, and HHC3K2 shows 62.5% of rate capability.

HHC9K4 shows extremely high supercapacitive performance in 3 electrode setup. It reveals the optimized structure which has balanced graphitic and porous phases along with the presence of heteroatom. Fig. 6 shows the schematic diagram for the various factors involve for the extremely high capacitance value of HHC9K4. The nanosheets (as shown by SEM and AFM in Fig. 2a and b) provide intercalation of electrolytic ions between the sheets which increase the ion adsorption sites. The presence of graphitic plane (shown by TEM in Fig. 2e) improved the conductivity of the material. Interconnected pores provide fast ionic transportation and lower the resistance. High BET surface area of 1548 m^2 g^{-1} (shown in Fig. 3a) provide more amount of ions to get adsorbed at the electrode surface. Hierarchical porous structure (as shown in Figs. 2d and 3b) promotes the ease in the diffusion of ions even at a high scan rate, which improves the rate capability [29]. The presence of nitrogen, oxygen and sulfur functionalities (confirmed by XPS) contribute to additional pseudocapacitance, improving the wettability and electrical conductivity of electrolytic ions

towards the electrode.

4.3.1. Device fabrication and cyclic performance retention

Further, for the practical application of the electrode materials, the symmetric supercapacitor devices are fabricated using an equal mass of the active material on two steel plates separating them bya filter paper soaked in 6 M KOH electrolyte. The schematic presentation of the fabrication of a symmetric supercapacitor is shown in Fig. 7a. The two-electrode electrochemical performance of the devices is evaluated through the CV, GCD, and EIS analyses. The comparative CV curves of the supercapacitor devices of the KOH activated carbons at a scan rate of 50 mV s^{-1} are shown in Fig. 7b. Here also, HHC9K4 based supercapacitor shows the highest area under the curve, which depicts the best capacitive performance among all the KOH activated samples. Whereas, HHC3K2 and HHC9K2 shows moderate performance. Two broad humps at 0.6 and 0.4 V in HHC3K2 indicate the presence of active sites which had undergone redox reversible reaction. The CV curves of HHC3K2 and HHC9K2 at different scan rates are shown in Fig. S1la and b, respectively. Fig. 7c shows the GCD plot of the activated carbons at a current density of 1 A g^{-1}, where all samples show near to linear behavior. The gravimetric electrode capacitance of supercapacitor devices is calculated using equation S(2). HHC9K4, HHC9K2, HHC3K4 and HHC3K2 show electrode specific capacitance of 550, 216, 33.5, and 183.5 Fg^{-1} at a current density of 1 A g^{-1}, respectively. The GCD curves of HHC3K2 and HHC9K2 at different current densities are shown in Figs. Slic and d, respectively. Fig. 7d shows that HHC9K4 possess excellent rate capability of 66% even at a high current density of 25 A g^{-1}.

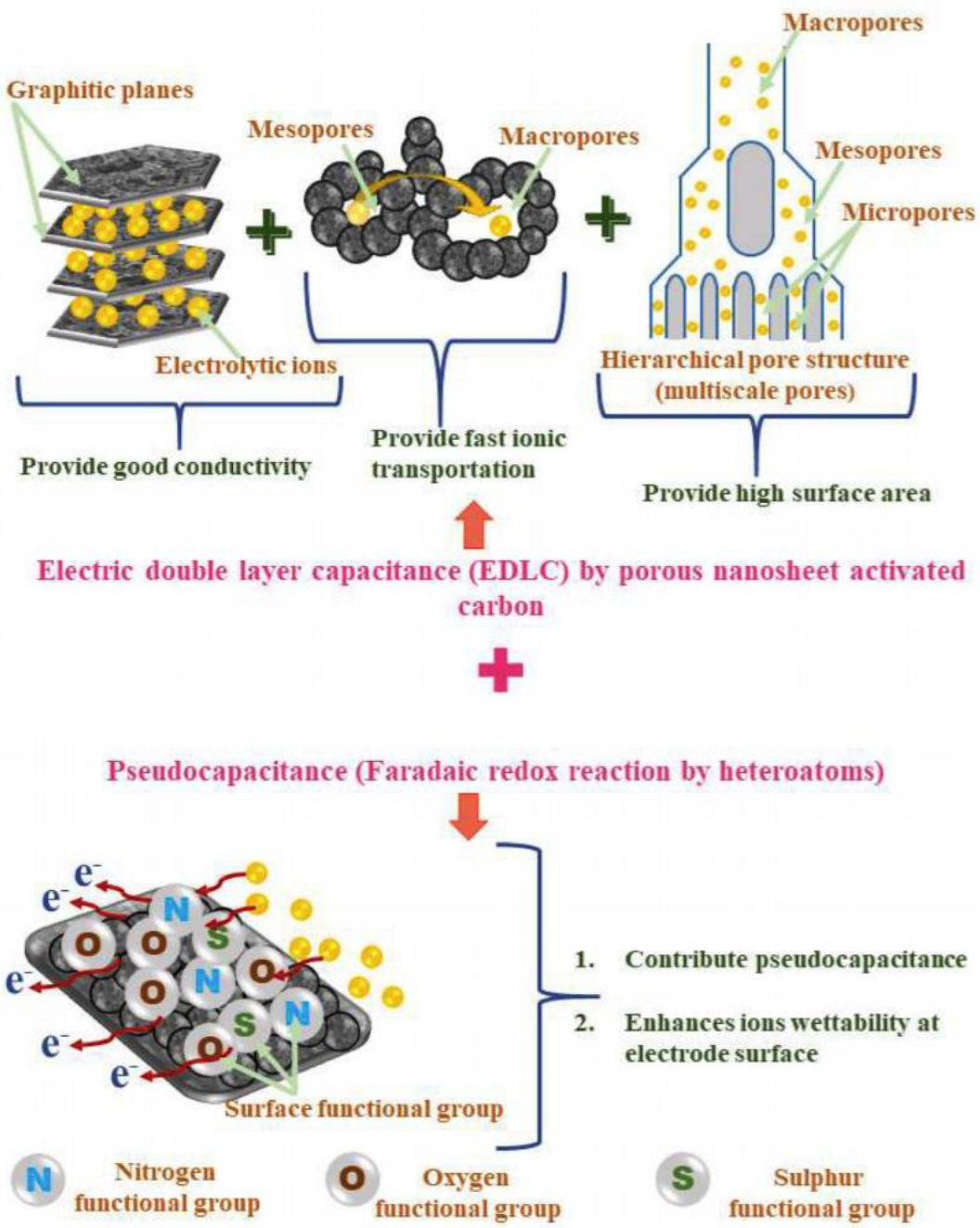

Fig. 6. Schematic representation of the contribution of various mechanistic approaches that results in extremely high capacitance in HHC9K4.

EIS measurements are also carried out to observe the conductivity and electron transfer rate of the activated carbons over a frequency range of 0.1—105 Hz. Fig. 8a shows the Nyquist plots of KOH activated carbons, where the x-intercept at high-frequency range represents the internal resistance, which includes intrinsic resistance of the electrode, the

contact resistance between the electrode and current collector, and ionic resistance of the electrolyte [83]. It is found to be 0.53, 0.53, 0.51, and 0.47 Ω for HHC9K4, HHC9K2, HHC3K4, and HHC3K2 based symmetric supercapacitor, respectively demonstrate very low equivalent series resistance. HHC9K4, HHC9K2, and HHC3K2 display small semicircle at high-frequency region followed by transformation to linearity at low-frequency region. The presence of semicircle can be attributed to the Faradaic process of charge transfer at the electrode-electrolyte interface. The length of the semicircle gives the charge transfer resistance, which is found to be 3.09 Ω for HHC9K4. In HHC9K4, a 45° line in the intermediate frequency region is called as Warburg impedance. This resembles the ion diffusivity into the pores of the electrode material [84]. Also, the vertical line of HHC9K4, close to 90° at low frequency suggests pure capacitive behavior and fast ionic transfer characteristics. This shows that the material possesses very low internal resistance, which results in high electrical conductivity [47,85]. Fig. 8b depicts the Bode phase of KOH activated samples. At high frequency, the phase angle is less than zero. On decreasing frequency, a hump can be seen which is due to the diffusive resistance of the devices. The phase angle sharply increases in decreasing the frequency from 50 to 0.1 Hz. The maximum phase angle obtained is 67, 57, 73, and 49° for HHC9K4, HHC9K2, HHC3K4, and HHC3K2 based symmetric supercapacitor at a low frequency of 0.1 Hz. These values are relatively lower than 90° due to the presence of pseudocapacitance. Fig. 8c shows the real capacitance of KOH activated samples [83,84], which is calculated using equation S(6). The HHC9K4 shows a much higher capacitance of 98 F g^{-1} at 0.1 Hz than other KOH activated samples. The capacitance decreases to zero after 10 Hz. This is due to the porous nature of the samples as the deep inner pore cannot be accessed by electrolytic ions at higher frequency [84,86]. The imaginary capacitance of KOH activated samples are calculated using equation S(7). Fig. 8d shows the imaginary capacitance vs. frequency plot where HHC9K4 shows maxima at 0.3 Hz. The corresponding relaxation time is 3.3 s. Relaxation time provide quantitative measures for the device on how fast charge and discharge reversibly. It also informs that the time needed to discharge all the energy with 50% efficiency from the device [83]. The shorter relaxation time of 3.3 s HHC9K4 shows excellent charge-discharge reversibility over other samples. The fast frequency response of HHC9K4 further confirms the interconnected hierarchical porous nanosheets structure [83,84].

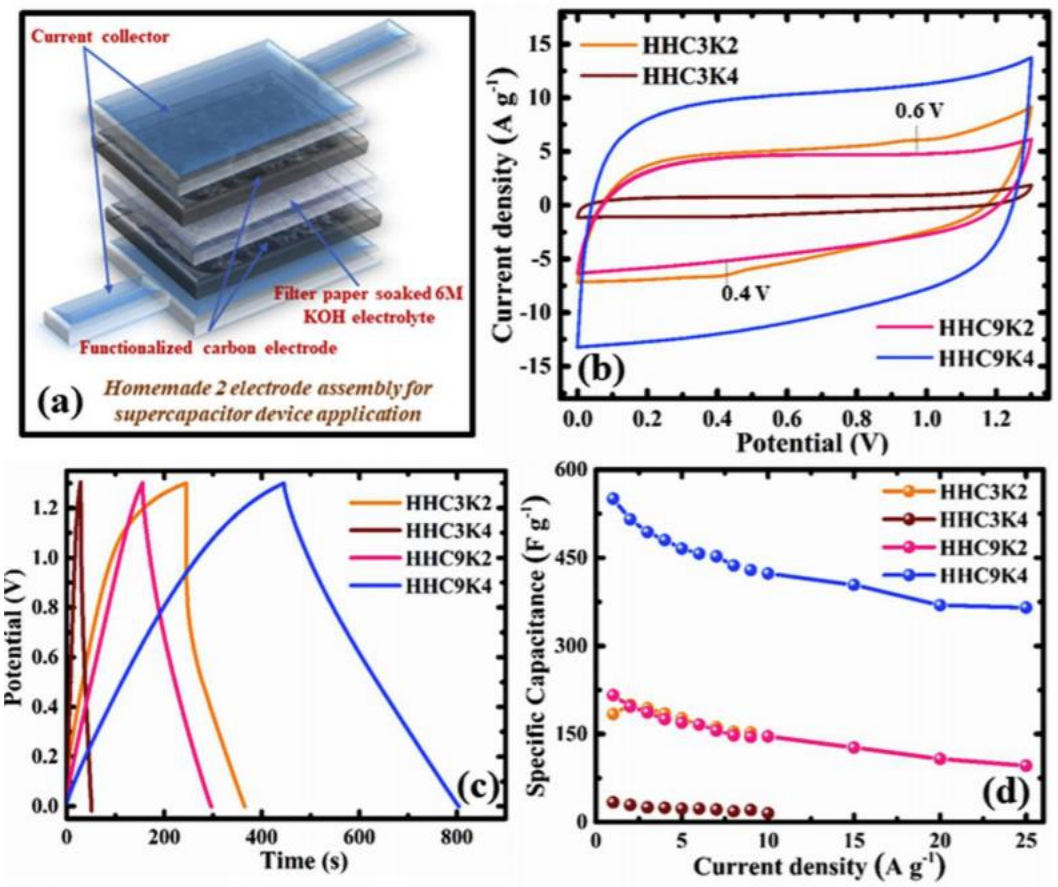

Fig. 7. (a) 2 electrode assembly for supercapacitor device application, (b) CV curve at 50 mV s^{-1}, (c) GCD at current density 1 A g^{-1}, and (d) gravimetric capacitance of KOH activated samples over different current density.

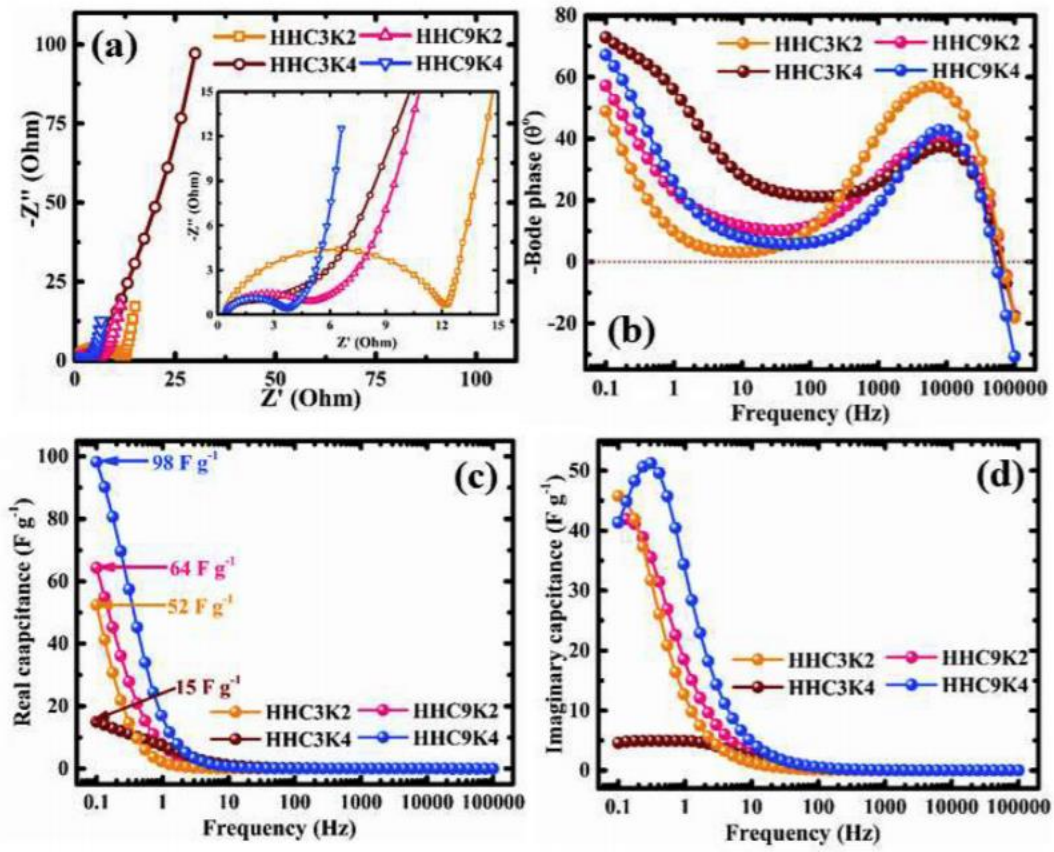

Fig. 8. (a) Nyquist plot (inset: magnified plot in higher frequency range), (b) Bode plot, (c) real capacitance (C') and (d) imaginary capacitance (C") parts of capacitance values for symmetric KOH activated electrode device.

HHC9K4 shows superior capacitance over other samples. So, the electrochemical analysis has been discussed further in detail. Fig. 9a shows the CV curves of the HHC9K4 symmetric supercapacitor at a scan rate of 50 mV s"! in different voltage windows. It is clear that the CV curves keep a rectangular-like shape and no obvious increase of anodic current at 1.3 V and rapid increase of anodic current at 2.0 V, indicating that the symmetric supercapacitor can be reversibly cycled within the voltage window up to 1.3 V. The increase in anodic current after 1.3 V potential resembles the initiation of Faradaic water decomposition [87]. Generally, higher energy densities are achieved using an organic electrolyte, operating at up to 3 V, but aqueous electrolytes are preferred for cost-effectiveness, chemical stability, and ease in handling. Most of the carbon-based electrodes are limited till potential of 0.7—1.0 V in aqueous electrolyte [9,22,30,51,55]. It is observed that HHC9K4 shows good stability even at 1.3 V [27]. Fig. S12 shows the comparative study of HHC9K4 assembled symmetric supercapacitor tested in the different potential ranges of O—1 V and O—1.3 V. Figs. S12a and b show the CV plot at different scan rates and GCD plots at various current density, respectively. Here, both the curve show excellent reversibility. Fig. S12c depict that symmetric supercapacitor at working potential of O—1.3 V shows better coulombic efficiency with an increment of 24% at a current density of 1 Ag! and around 9% at a

current density of 10 A g' as compared to the device having the working potential of O—1 V. However, iR drops remains almost similar till current density of 10 A g~ |, but at higher current density iR drop increases to 13% for device working at O—1 V, as shown in Fig. S12d. This show better rate capability of HHC9K4 symmetric device working at the potential range of O—1.3 V. Also, 39% increment is observed in specific capacitance value for device working at O—1.3 V as compared to the device having the potential of O—1 V, as shown in Fig. S12e. It is well known that energy density strongly depends upon the working potential of the device. In this vein, energy density significantly increases to 32.3 Wh Kg~! at a power density of 325 W kg~! for device potential of OQ—1.3 V, whereas, the energy density of 13.8 Wh Kg™! at power density 250 W kg™! is delivered by a device having the working potential of O—1 V, as depicted in Fig. S12f. Fig. 9b shows the CV curves for HHC9K4 at 100, 80, 50, 30, and 10 mV s"! scan rates, where excellent material stability and reversibility can be seen by observing identical CV curves even at a very high scan rate. This indicates low internal resistance, fast kinetics for double layer formation, and good rate capability due to interconnected hierarchical porous carbon nanosheets network. The quasi-linear behavior in GCD analysis (as shown in Fig. 9c) further reveals the near EDLC behavior of the activated carbon HHC9K4, which is in good agreement with the CV measurement result. A potential limit of 1.3 V was defined to minimize the iR drop and increase the coulombic efficiency. Fig. 9d shows coulombic efficiency versus current density plot for HHC9K4 where the coulombic efficiency is 80% at a current density of 1 Ag^{-1} which gradually increases to 100% around the current density of 10 A^{-1}. The coulombic efficiency is calculated using equation S(3). This shows that the charge-discharge process occurs with less charge loss in the material indicating excellent supercapacitive performance. iR drop plot in Fig. 9d suggests that the material shows very less internal resistance and high conductivity. Again, energy and power densities are the most important factors for the practical application of a supercapacitor device. The energy and power density of KOH activated samples are calculated using equations S4 and S5, respectively. Fig. 9e shows the Ragone plots of various KOH activated carbon-based symmetric supercapacitors. The plot shows that the HHC9K4 supercapacitor assembly exhibits excellent energy and power densities as compared to other KOH activated samples. It delivers a maximum energy density of 32 W h Kg^{-1} at a power density of 325 W Kg^{-1} It also maintains up to 21.4 W h Kg^{-1} even at a very high-power density of 8125 W Kg^{-1} The results are excellent compared to the reported literature [46—48].

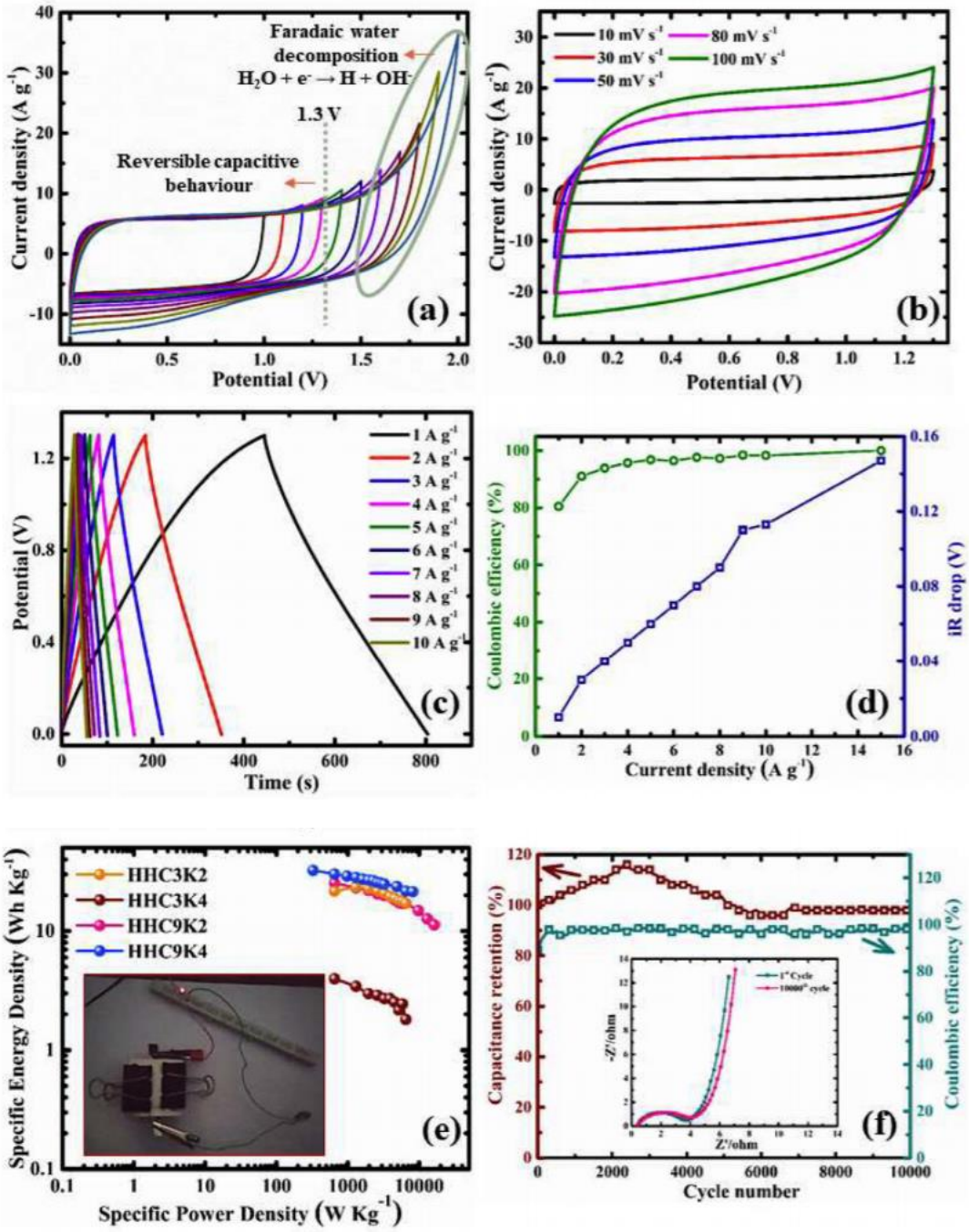

Fig. 9. (a) CV curves of HHC9K4 at 50 mV s^{-1} at the different potential window, (b) CV curves of HHC9K4 at different scan rates, (c) GCD curves of HHC9K4 at different current densities, (d) coulombic efficiency and IR (voltage) drop of HHC9K4 at different current densities, (e) Ragone plots for KOH activated samples, inset: digital micrograph of lightning of LED by an assembled supercapacitor, and (f) cyclic stability performance for the symmetric supercapacitor derived from HHC9K4 using continuous GCD cycles up to 10,000 at a current density of 5 A g^{-1}, inset: EIS curves of HHC9K4 before and after 10,000 cycles.

Further, long cycle life is a crucial requirement for a high- performance supercapacitor device. Fig. 9f represents the cyclic stability of the HHC9K4 based symmetric supercapacitor device at a current density of 5 A g^{-1} using continuous GCD cycles. The supercapacitor shows excellent cyclic stability by the retention of 98% of its initial capacitance even after 10,000 GCD cycles at a current density of 5 A g^{-1}. Although, there is an increase in capacitance till ~3000th cycle, which suggests the diffusion of electrolytic ions at electrode pores. Also, Fig. 9f shows that the coulombic efficiency increases with the growth of cycle numbers and then remains constant which suggests easy adsorption and desorption during charge-discharge cycles. Inset of Fig. 9f, show Nyquist plots of HHC9K4 before and after 10,000th cycles. The result shows a little increment in internal as well as charge transfer resistance after the 10,000th cycle due to a decrease in ions diffusion between electrode-electrolyte interfaces. The achieved overall electrochemical performance - specific capacitance, energy density, rate capability, and cyclic stability is also superior compared to the most of the reported biomass-derived activated carbons, for example corncob residue, soya, rice husk, wood, banana fibers, tremella, bamboo chopsticks, etc. as compared in Table 4.

4.3.2. Design of flexible supercapacitor

There has been a rise in demand for flexible energy storage devices for portable electronics and this work represents a simple and cost-effective approach to achieve the same [58,96]. The fabrication of a flexible supercapacitor is discussed in the characterization section 3.3. The schematic representation of asassembled flexible device is shown in Fig. 10a. The CV curves at different scan rate and GCD curves at different current densities of as-assembled flexible supercapacitor using HHC9K4 as electrode material are shown in Figs. S13a and b, respectively. Fig. 1Ob shows the CV plots of flexible devices in straight and bending mode at a scan rate of 50 mV s^{-1}. The curve implies that there is very little deviation when the device is tested in bending mode. Similarly, a slight variation in rate capability is observed from straight to bending mode as shown in Fig. 10c. The inset of Fig. 10c shows the digital photograph of a flexible supercapacitor tested in bending mode. The specific capacitance achieved is 145 mF cm^{-1} at a current density of 0.8 mA cm^{-1}. The capacitance achieved is due to the synergistic contribution of redox active solid state electrolyte KOH PVA-K_3FeCN_6 and HHC9K4 activated carbon electrode. At last, the stability of the flexible device is tested using continuous chargedischarge cycles at a current density of 0.8 mA cm^{-1}, where 95% capacitance retention is observed till 500 cycles, after which the device is tested in bending mode, which shows 82% capacitance retention till 1000 charge-discharge cycles as shown in Fig. 10d. Inset in Fig. 10d shows the GCD plot of before and after cycle life.

Table 4

Comparative electrochemical performance of different studied supercapacitor or supercapacitor electrodes based on biomass-derived activated carbons with the present work.

Activated carbons	System studied	Specific capacitance	Energy density	Cyclic stability	Ref. no.
Human hair (HHC9K4)	Both 3 & 2 electrode systems	999 F g^{-1} at 1 A g^{-1}	32 W h Kg^{-1} at 325 W Kg^{-1}	98% at 5 A g^{-1} after 10,000 GCD cycles	Present work
Human hair	Both 3 & 2 electrode systems	340 F g^{-1} at 1 A g^{-1}	29 W h Kg^{-1} at 2243 W Kg^{-1}	98% at 5 A g^{-1} after 20,000 GCD cycles	[47]
Human hair	2 electrode system	115 F g^{-1} at 0.1 A g^{-1}	19.2 Wh Kg^{-1}	–	[46]
Elm seeds	3 electrode system	501 F g^{-1} at 1 A g^{-1}	18.6 Wh kg^{-1} at 1310 W kg^{-1}	90.8% after 10,000 GCD cycles	[88]
Soya	3 electrode system	425 F g^{-1}	–	91% after 10,000 CV cycles	[89]
Corncob residue	Both 3 & 2 electrode system	120 F g^{-1} at 1 A g^{-1}	5.3 W h Kg^{-1} at 8276 W Kg^{-1}	100% at 1 A g^{-1} after 1,00,000 GCD cycles	[32]
Animal bone	2 electrode system	185 F g^{-1} at 0.05 A g^{-1}	–	–	[90]
Soya	3 electrode system	193 F g^{-1} at 0.5 A g^{-1}	24.3 W h Kg^{-1} at 750 W Kg^{-1}	93% at 10 A g^{-1} after 10,000 GCD cycles	[13]
Waste tea leaves	3 electrode system	330 F g^{-1} at 1 A g^{-1}	–	92% at 5 A g^{-1} after 2000 GCD cycles	[85]
Rice husk	2 electrode system	245 F g^{-1} at 0.05 A g^{-1}	8.36 W h Kg^{-1}	99% at 0.05 A g^{-1} after 1000 GCD cycles	[91]
Rice husk	2 electrode system	147 F g^{-1} at 0.1 A g^{-1}	5.11 W h Kg^{-1}	85% at 1 A g^{-1} after 10,000 GCD cycles	[92]
Wood	3 electrode system	118.7 F g^{-1} at 1 A g^{-1}	–	–	[93]
Bamboo	Both 3 & 2 electrode system	301 F g^{-1} at 0.1 A g^{-1}	6.1 W h Kg^{-1} at 26000 W Kg^{-1}	100% retention 20,000 at 1 A g^{-1} GCD cycles.	[77]
Banana fibers	3 electrode system	74 F g^{-1} at 500 mA g^{-1}	–	88% at 500 mA g^{-1} after 500 GCD cycles	[26]
Fish gill	3 electrode system	334 F g^{-1} at 2 A g^{-1}	11.2 W h Kg^{-1} at 125 W Kg^{-1}	98% at 2 A g^{-1} after 10,000 GCD cycles	[34]
Chicken feather	Both 3 & 2 electrode system	302 F g^{-1} at 1 A g^{-1}	7.98 W h Kg^{-1} at 1400 W Kg^{-1}	83% at 1 A g^{-1} after 5000 GCD cycles	[40]
Bagasse wastes	Both 3 & 2 electrode system	320 F g^{-1} at 0.5 A g^{-1}	6.25 W h Kg^{-1} at 100.5 W Kg^{-1}	92.85% at 10 A g^{-1} after 15,000 GCD cycles	[94]
Carton box	2 electrode system	311 F g^{-1} at 0.5 A g^{-1}	10.8 W h Kg^{-1} at 125 W Kg^{-1}	96.4% at 8 A g^{-1} after 5000 GCD cycles	[95]
Cotton stalk	Both 3 & 2 electrode system	254 F g^{-1} at 0.2 A g^{-1}	18.14 W h Kg^{-1} at 450.37 W Kg^{-1}	96% at 1 A g^{-1} after 10,000 GCD cycles	[51]
Tremella	Both 3 & 2 electrode system	71 F g^{-1} at 1 A g^{-1}	9.6 W h Kg^{-1} at 124 W Kg^{-1}	94% at 5 A g^{-1} after 10,000 GCD cycles	[30]
Bamboo chopsticks	3 electrode system	212 F g^{-1} at 0.1 A g^{-1}	–	96% at 1 A g^{-1} after 1000 GCD cycles	[31]

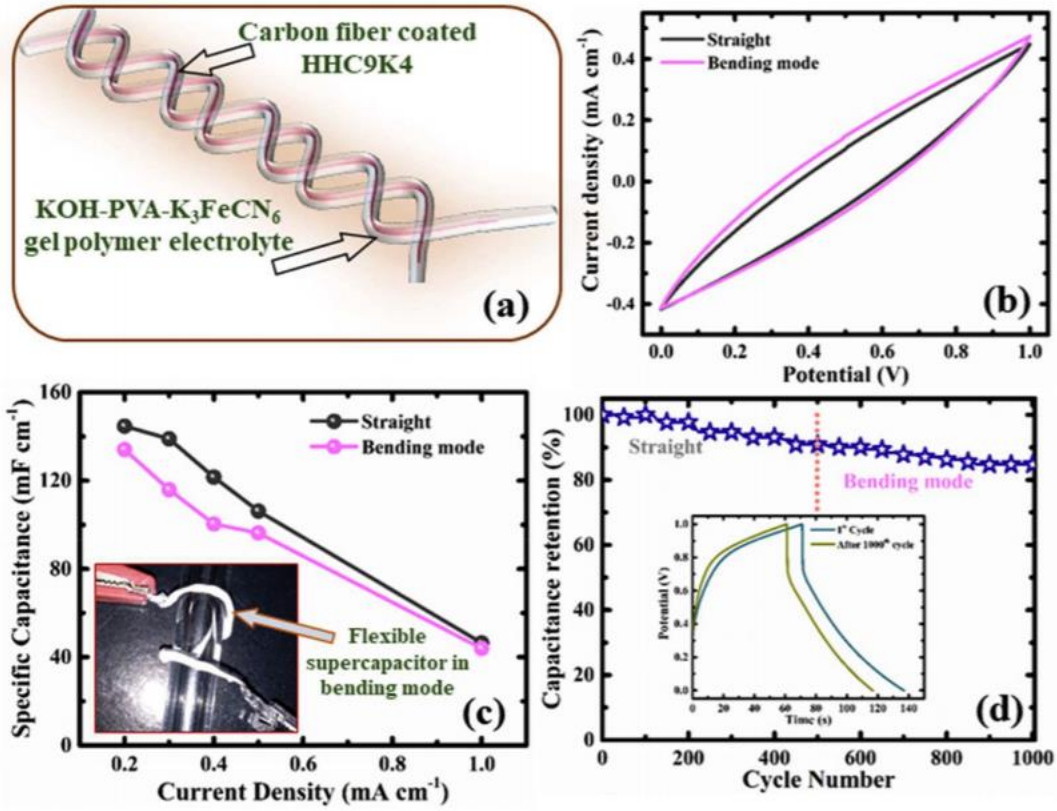

Fig. 10. (a) CV curve at a scan rate of 50 mV s^{-1}, (b) GCD curve at current density 1 A g^{-1} in straight and bending mode, inset: digital photograph of flexible supercapacitor tested in bending mode, (c) schematic of the assembly of the flexible supercapacitor, and (d) cycle life of flexible supercapacitor at current density 0.8 mA cm^{-1} till 1000 cycles.

5. Conclusions

The study demonstrates a waste biomass derived interconnected, hierarchically porous,

heteroatom doped carbon nanosheets for high-performance supercapacitor. It reveals that the different chemical activators (H_3PO_4, $ZnCl_2$, and KOH) result in different morphologies and properties of activated carbon. Among all the activators, KOH activation shows superior electrochemical performance. Further study on KOH activation is carried out using different carbonization temperatures and the KOH impregnation ratio. Herein, an optimized sample is synthesized using modified carbonization and activation. The modified synthesis step results in extremely high porous carbon nanosheets having a specific surface area of 1548 $m^2\ g^{-1}$. Also, a high amount of heteroatom content of around 25% is obtained by XPS analysis. The microscopic analyses depict a sheet size of 50—200 nm, having sheet thickness ranging from 15 to 27 nm. Thus, the electrode material prepared from KOH activated carbon (HHC9K4) displays an outstanding specific capacitance value of 999 F g^{-1} at a current density of 1 Ag^{-1} The assembled symmetric supercapacitor derived from it also delivers an excellent energy density of 32 W h Kg^{-1} at a power density of 325 W Kg^{-1} and retains up to 21.4 W h Kg^{-1} even at a very highpower density of 8125 W Kg^{-1}. Moreover, it exhibits a high cyclic stability by retaining 98% of its initial capacitance value after 10,000 continuous GCD cycles at a high current density of 5 Ag^{-1} using 6 M KOH as the electrolyte. Flexible supercapacitor device using redox active gel electrolyte shows a synergistic specific capacitance of 145 mF cm^{-1} at a current density of 0.8 mA cm^{-1} having very little deviation in bending mode. The performance of the studied supercapacitor can be attributed to the (a) unique interconnected nanosheets, (b) hierarchical porous structure, (c) successful incorporation of the heteroatoms in carbon nanosheets. This facilitates a large amount of charge accumulation and reduces the ion diffusion path thereby reducing internal resistance. The presence of heteroatoms provides additional pseudocapacitance via reversible redox reactions and enhance the conductivity of carbon material. Therefore, the present work successfully presents an_ interconnected hierarchical porous heteroatom doped carbon nanosheets from waste biomass for use in advanced energy storage application.

Associated content

Supporting Information. Schematic of human hair derived KOH activated samples; Equation used for calculation of electrochemical parameters, TGA thermogram of HHs; SEM micrograph of HHC3, HHC9, HHC9P4, HHC9Z4, HHC9K2, HHC3K2, and HHC3K4; Three dimensional AFM image and height profile of HHC9K4; TEM and HRTEM micrograph of) HHC3, HHC9, HHC3K2, HHC3K4, HHC9K2, HHC9K4; Nitrogen adsorption and desorption isotherm for HHC9, HHC9Z4, and HHC9P4; Raman spectra, XRD pattern and XPS spectra of HHC9P4 and HHC9Z4; Surface area, pore volume and pore diameter of human hair derived HHC9, HHC9Z4, and HHC9P4; Deconvolution of XPS spectra of C 1s, O 1s, N 1s and S 2p for HHC9P4, HHC9Z4 HHC, HHC3K2 and HHC3K4; Summary of peak assignments for C 1s, N 1s, O 1s, and S 2p species of human hair, carbonized and activated samples; 3 electrode Electrochemical performance CV curve at scan rate 50 mV s^{-1} GCD curve at current density 1 A g^{-1}, EIS and gravimetric capacitance at different current density for HHC9, HHC9P4, HHC9Z4 and HHC9K4; CV curve at different scan rate and GCD curves at different current

densities for HHC3K2 and HHC3K4, respectively in three electrode system and two electrode system; comparative electrochemical studies of HHC9K4 based symmetric device tested in different potential window, O—1 V and O—1.3 V; CV curve at different scan rates and GCD curves at different current densities of as- assembled flexible supercapacitor.

Credit author statement

Prerna Sinha: Conceptualization, Methodology, Validation, Investigation, Writing - original draft, Writing - review & editing, Visualization.

Amit Yadav: Assisted in electrochemical studies.

Alekha Tyagi: Performed AFM and review manuscript.

Pradip Paik: Supervision regarding, SEM, TEM and BET studies.

Hiroyuki Yokoi: Supervision.

Amit Naskar: Supervision.

Tapas Kuila: Supervision.

Kamal K. Kar: Resources, Writing - review & editing, Visualization, Supervision.

Declaration of competing interest

The authors declare that they have no known competing financial interests or personal relationships that could have appeared to influence the work reported in this paper.

Acknowledgements

The authors would like to thank IMPRINT Proposal-6134 (Ministry of Textiles and Ministry of Human Resource Development) Government of India for their support to carry on this present research.

Appendix A. Supplementary data

Supplementary data to this article can be found online at https://doi.org/10.1016/j.carbon.2020.07.007.

References

1. L.L. Zhang, X.S. Zhao, Carbon-based materials as supercapacitor electrodes, Chem. Soc. Rev. 38 (2009) 2520, https://doi.org/10.1039/b81 3846).
2. V.V.N. Obreja, On the performance of supercapacitors with electrodes based on carbon nanotubes and carbon activated material-A review, Phys. E Low Dimension. Syst. Nanostruct. 40 (2008) 2596—2605, https://doi.org/10.1016/ j.physe.2007.09.044.
3. S.K. Singh, M.J. Akhtar, K.K. Kar, Hierarchical carbon nanotube-coated carbon fiber: ultra lightweight, thin, and highly efficient microwave absorber, ACS Appl. Mater. Interfaces 10 (2018) 24816-24828, https://doi.org/10.1021/ acsami.8b06673.
4. M. Rana, G. Arora, U.K. Gautam, N- and S-doped high surface area carbon derived from soya chunks as scalable and efficient electrocatalysts for oxygen reduction, Sci. Technol. Adv. Mater. 16 (2015) 14803, https://doi.org/10.1088/ 1468-6996/16/1/014803.
5. J. Li, K. Liu, X. Gao, B. Yao, K. Huo, Y. Cheng, X. Cheng, D. Chen, B. Wang, W. Sun, D. Ding, M. Liu, L. Huang, Oxygen- and nitrogen-enriched 3D porous carbon for supercapacitors of high volumetric capacity, ACS Appl. Mater. Interfaces 7 (2015) 24622—24628, https://doi.org/10.1021/acsami.5b06698.
6. W. Sun, S.M. Lipka, C. Swartz, D. Williams, F. Yang, Hemp-derived activated carbons for supercapacitors, Carbon 103 (2016) 181—192, https://doi.org/ 10.1016/j.carbon.2016.02.090.
7. F.K. Yuen, B.H. Hameed, Recent developments in the preparation and regeneration of activated carbons by microwaves, Adv. Colloid Interface Sci. 149 (2009) 19—27, https://doi.org/10.1016/j.cis.2008.12.005.
8. B. Hu, K. Wang, L. Wu, S.H. Yu, M. Antonietti, M.M. Titirici, Engineering carbon materials from the hydrothermal carbonization process of biomass, Adv. Mater. 22 (2010) 813-828, https://doi.org/10.1002/adma.2009028 12.
9. S. Roldan, I. Villar, V. Ruiz, C. Blanco, M. Granda, R. Menéndez, R. Santamaria, Comparison between electrochemical capacitors based on NaOH- and KOHactivated carbons, Energy Fuels 24 (2010) 3422-3428, https://doi.org/ 10.1021 /ef901538m.
10. T. Chen, S. Deng, B. Wang, J. Huang, Y. Wang, G. Yu, CO2 adsorption on crab shell derived activated carbons: contribution of micropores and nitrogencontaining groups, RSC Adv. 5 (2015) 48323—48330, https://doi.org/ 10.1039/C5RA04937G.
11. A. Tyagi, A. Yadav, P. Sinha, S. Singh, P. Paik, K.K. Kar, Chicken feather rachis: an improvement over feather fiber derived electrocatalyst for oxygen electroreduction, Appl. Surf. Sci. 495 (2019) 143603, https://doi.org/10.1016/ j.apsusc.2019.143603.
12. M.P. Elizalde-Gonzalez, V. Hernandez-Montoya, Characterization of mango pit as raw material in the preparation of activated carbon for wastewater treatment, Biochem. Eng. J. 36 (2007) 230—238, https://doi.org/10.1016/ j.bej.2007.02.025.
13. M. Rana, K. Subramani, M. Sathish, U.K. Gautam, Soya derived heteroatom doped carbon as a promising platform for oxygen reduction, supercapacitor and CO, capture, Carbon 114 (2017) 679-689, https://doi.org/10.1016/ j.carbon.2016.12.059.

14. X. Liu, W. Zhou, L. Yang, L. Li, Z. Zhang, Y. Ke, S. Chen, Nitrogen and sulfur codoped porous carbon derived from human hair as highly efficient metal-free electrocatalysts for hydrogen evolution reactions, J. Mater. Chem. A. 3 (2015) 8840-8846, https://doi.org/10.1039/C5TAO1 209K.
15. A. Gonzalez, E. Goikolea, J.A. Barrena, R. Mysyk, Review on supercapacitors: technologies and materials, Renew. Sustain. Energy Rev. 58 (2016) 1189—1206, https://doi.org/10.1016/j.rser.2015.12.249.
16. P. Yang, W. Mai, Flexible solid-state electrochemical supercapacitors, Nano Energy 8 (2014) 274—290, https://doi.org/10.1016/j.nanoen.2014.05.022.
17. Y. Zhai, Y. Dou, D. Zhao, P.F. Fulvio, R.T. Mayes, S. Dai, Carbon materials for chemical capacitive energy storage, Adv. Mater. 23 (2011) 4828—4850, https://doi.org/10.1002/adma.201100984.
18. M. Vangari, T. Pryor, L. Jiang, Supercapacitors: review of materials and fabrication methods, J. Energy Eng. 139 (2013) 72—79, https://doi.org/10.1061/ (ASCE)EY.1943-7897.0000102.
19. M. Zhou, J. Gomez, B. Li, Y.B. Jiang, S. Deng, Oil tea shell derived porous carbon with an extremely large specific surface area and modification with MnO; for high-performance supercapacitor electrodes, Appl. Mater. Today 7 (2017) 47—54, https://doi.org/10.1016/j.apmt.2017.01.008.
20. L. Zhu, F. Shen, R.L. Smith, L. Yan, L. Li, X. Qi, Black liquor-derived porous carbons from rice straw for high-performance supercapacitors, Chem. Eng. J. 316 (2017) 770—777, https://doi.org/10.1016/j.cej.2017.02.034.
21. M. Biswal, A. Banerjee, M. Deo, S. Ogale, From dead leaves to high energy density supercapacitors, Energy Environ. Sci. 6 (2013) 1249, https://doi.org/ 10.1039/c3ee22325f.
22. A.E. Ismanto, S. Wang, F.E. Soetaredjo, S. Ismadji, Preparation of capacitor's electrode from cassava peel waste, Bioresour. Technol. 101 (2010) 3534—3540, https://doi.org/10.1016/j.biortech.2009.12.123.
23. X. Li, W. Xing, S. Zhuo, J. Zhou, F. Li, S.Z. Qiao, G.Q. Lu, Preparation of capacitor's electrode from sunflower seed shell, Bioresour. Technol. 102 (2011) 1118—1123, https://doi.org/10.1016/j.biortech.2010.08.110.
24. H. Tan, X. Wang, D. Jia, P. Hao, Y. Sang, H. Liu, Structure-dependent electrode properties of hollow carbon micro-fibers derived from Platanus fruit and willow catkins for high-performance supercapacitors, J. Mater. Chem. A. 5 (2017) 2580—2591, https://doi.org/10.1039/C6TA10191G.
25. H. Zhu, J. Yin, X. Wang, H. Wang, X. Yang, Microorganism-derived heteroatom-doped carbon materials for oxygen reduction and_ supercapacitors, Adv. Funct. Mater. 23 (2013) 1305—1312, https://doi.org/10.1002/ adfm.201201643.
26. V. Subramanian, C. Luo, A.M. Stephan, K.S. Nahm, S. Thomas, B. Wei, Supercapacitors from activated carbon derived from banana fibers, J. Phys. Chem. C 111 (2007) 7527—7531, https://doi.org/10.1021 /jp067009t.

27. T.E. Rufford, D. Hulicova-Jurcakova, Z. Zhu, G.Q. Lu, Nanoporous carbon electrode from waste coffee beans for high performance supercapacitors, Electrochem. Commun. 10 (2008) 1594—1597, https://doi.org/10.1016/ j.elecom.2008.08.022.
28. K. Wang, R. Yan, N. Zhao, X. Tian, X. Li, S. Lei, Y. Song, Q. Guo, L. Liu, Bioinspired hollow activated carbon microtubes derived from willow catkins for supercapacitors with high volumetric performance, Mater. Lett. 174 (2016) 249—252, https://doi.org/10.1016/j.matlet.2016.03.063.
29. M. Gopiraman, D. Deng, B.S. Kim, I.M. Chung, I.S. Kim, Three-dimensional cheese-like carbon nanoarchitecture with tremendous surface area and pore construction derived from corn as superior electrode materials for supercapacitors, Appl. Surf. Sci. 409 (2017) 52—59, https://doi.org/10.1016/ j.apsusc.2017.02.209.
30. N. Guo, M. Li, X. Sun, F. Wang, R. Yang, Tremella derived ultrahigh specific surface area activated carbon for high performance supercapacitor, Mater. Chem. Phys. 201 (2017) 399—407, https://doi.org/10.1016/ j.matchemphys.201 7.08.054.
31. G. Zhang, H. Chen, W. Liu, D. Wang, Y. Wang, Bamboo chopsticks-derived porous carbon microtubes/flakes composites for supercapacitor electrodes, Mater. Lett. 185 (2016) 359-362, https://doi.org/10.1016/ j.matlet.2016.09.045.
32. W.-H. Qu, Y.-Y. Xu, A.-H. Lu, X.-Q. Zhang, W.-C. Li, Converting biowaste corncob residue into high value added porous carbon for supercapacitor electrodes, Bioresour. Technol. 189 (2015) 285—291, https://doi.org/10.1016/ j.biortech.2015.04.005.
33. W. Chen, H. Zhang, Y. Huang, W. Wang, A fish scale based hierarchical lamellar porous carbon material obtained using a natural template for high performance electrochemical capacitors, J. Mater. Chem. 20 (2010) 4773—4775, https://doi.org/10.1039/c0Ojm00382d.
34. Y. Han, N. Shen, S. Zhang, D. Li, X. Li, Fish gill-derived activated carbon for supercapacitor application, J. Alloys Compd. 694 (2017) 636—642, https:// doi.org/10.1016/j.jallcom.2016.10.013.
35. R. Wang, P. Wang, X. Yan, J. Lang, C. Peng, Q. Xue, Promising porous carbon derived from celtuce leaves with outstanding supercapacitance and CO2 capture performance, ACS Appl. Mater. Interfaces 4 (2012) 5800—5806, https://doi.org/10.1021/am302077c.
36. J. Deng, T. Xiong, F. Xu, M. Li, C. Han, Y. Gong, H. Wang, Y. Wang, Inspired by bread leavening: one-pot synthesis of hierarchically porous carbon for supercapacitors, Green Chem. 17 (2015) 4053—4060, https://doi.org/10.1039/ C5GC00523].
37. K.N. Chaudhari, M.Y. Song, J.S. Yu, Transforming hair into heteroatom-doped carbon with high surface area, Small 10 (2014) 2625—2636, https://doi.org/ 10.1002/smll.201303831.
38. L. Kreplak, A. Franbourg, F. Briki, F. Leroy, D. Dallé, J. Doucet, A new deformation model of hard «-keratin fibers at the nanometer scale: implications for hard a-keratin intermediate filament mechanical properties, Biophys. J. 82 (2002) 2265—2274, https://doi.org/10.1016/SO006-3495(02)75572-0.

39. J.W.S. Hearle, A critical review of the structural mechanics of wool and hair fibres, Int. J. Biol. Macromol. 27 (2000) 123-138, https://doi.org/10.1016/ S0141-8130(00)00116-1.
40. Q. Wang, Q. Cao, X. Wang, B. Jing, H. Kuang, L. Zhou, A high-capacity carbon prepared from renewable chicken feather biopolymer for supercapacitors, J. Power Sources 225 (2013) 101-107, https://doi.org/10.1016/ j.jjpowsour.2012.10.022.
41. B. Pramanick, L.B. Cadenas, D.-M. Kim, W. Lee, Y.-B. Shim, S.O. MartinezChapa, M.J. Madou, H. Hwang, Human hair-derived hollow carbon microfibers for electrochemical sensing, Carbon 107 (2016) 872—877, https://doi.org/ 10.1016/j.carbon.2016.06.095.
42. Z.-Q. Zhao, P.-W. Xiao, L. Zhao, Y. Liu, B.-H. Han, Human hair-derived nitrogen and sulfur co-doped porous carbon materials for gas adsorption, RSC Adv. 5 (2015) 73980—73988, https://doi.org/10.1039/C5RA15690D.
43. M.J. Ahmed, M.A. Islam, M. Asif, B.H. Hameed, Human hair-derived high surface area porous carbon material for the adsorption isotherm and kinetics of tetracycline antibiotics, Bioresour. Technol. 243 (2017) 778—784, https:// doi.org/10.1016/j.biortech.2017.06.174.
44. A. Sahasrabudhe, S. Kapri, S. Bhattacharyya, Graphitic porous carbon derived from human hair as 'green' counter electrode in quantum dot sensitized solar cells, Carbon 107 (2016) 395—404, https://doi.org/10.1016/ j.carbon.2016.06.015.
45. H. Dong, H. Zhang, Y. Xu, C. Zhao, Facile synthesis of a-Fe203 nanoparticles on porous human hair-derived carbon as improved anode materials for lithium ion batteries, J. Power Sources 300 (2015) 104—111, https://doi.org/10.1016/j.jpowsour.2015.09.057.
46. R. Satish, A. Vanchiappan, C.L. Wong, K.W. Ng, M. Srinivasan, Macroporous carbon from human hair: a journey towards the fabrication of high energy Liion capacitors, Electrochim. Acta 182 (2015) 474—481, https://doi.org/ 10.1016/j.electacta.2015.09.127.
47. W. Qian, F. Sun, Y. Xu, L. Qiu, C. Liu, S. Wang, F. Yan, Human hair-derived carbon flakes for electrochemical supercapacitors, Energy Environ. Sci. 7 (2014) 379—386, https: //doi.org/10.1039/C3EE43111H.
48. W. Si, J. Zhou, S. Zhang, S. Li, W. Xing, S. Zhuo, Tunable N-doped or dual N, Sdoped activated hydrothermal carbons derived from human hair and glucose for supercapacitor applications, Electrochim. Acta 107 (2013) 397-405, https://doi.org/10.1016/j.electacta.2013.06.065.
49. D. Bhattacharjya, J.-S. Yu, Activated carbon made from cow dung as electrode material for electrochemical double layer capacitor, J. Power Sources 262 (2014) 224—231, https://doi.org/10.1016/j.jpowsour.2014.03.143.
50. H. Wang, Z. Xu, A. Kohandehghan, Z. Li, K. Cui, X. Tan, TJ. Stephenson, C.K. King'Ondu, C.M.B. Holt, B.C. Olsen, J.K. Tak, D. Harfield, A.O. Anyia, D. Mitlin, Interconnected carbon nanosheets derived from hemp for ultrafast supercapacitors with high energy, ACS Nano 7 (2013) 5131—5141, https:// doi.org/10.1021/nn400731g.

51. X. Tian, H. Ma, Z. Li, S. Yan, L. Ma, F. Yu, G. Wang, X. Guo, Y. Ma, C. Wong, Flute type micropores activated carbon from cotton stalk for high performance supercapacitors, J. Power Sources 359 (2017) 88—96, https://doi.org/10.1016/ j.jjpowsour.2017.05.054.
52. S.K. Singh, H. Prakash, M.J. Akhtar, K.K. Kar, Lightweight and highperformance microwave absorbing heteroatom-doped carbon derived from chicken feather fibers, ACS Sustain. Chem. Eng. 6 (2018) 5381—5393, https:// doi.org/10.1021/acssuschemeng.8b00183.
53. J. Hou, C. Cao, F. Idrees, X. Ma, Hierarchical porous nitrogen-doped carbon nanosheets derived from silk for ultrahigh-capacity battery anodes and supercapacitors, ACS Nano 9 (2015) 2556—2564, https://doi.org/10.1021/ nn506394r.
54. Y. He, X. Zhuang, C. Lei, L. Lei, Y. Hou, Y. Mai, X. Feng, Porous carbon nanosheets: synthetic strategies and electrochemical energy related applications, Nano Today 24 (2019) 103-119, https://doi.org/10.1016/ j-nantod.2018.12.004.
55. Y.S. Yun, S.Y. Cho, J. Shim, B.H. Kim, S.J. Chang, S.J. Baek, Y.S. Huh, Y. Tak, Y.W. Park, S. Park, H.J. Jin, Microporous carbon nanoplates from regenerated silk proteins for supercapacitors, Adv. Mater. 25 (2013) 1993—1998, https:// doi.org/10.1002/adma.201204692.
56. C. Long, X. Chen, L. Jiang, L. Zhi, Z. Fan, Porous layer-stacking carbon derived from in-built template in biomass for high volumetric performance supercapacitors, Nano Energy 12 (2015) 141-151, https://doi.org/10.1016/ j.nanoen.2014.12.014.
57. G. Ma, J. Li, K. Sun, H. Peng, J. Mu, Z. Lei, High performance solid-state supercapacitor with PVA—KOH—K3[Fe(CN).] gel polymer as electrolyte and separator, J. Power Sources 256 (2014) 281-287, https://doi.org/10.1016/ j.jjpowsour.2014.01.062.
58. B. De, A. Yadav, S. Khan, K.K. Kar, A facile methodology for the development of a printable and flexible all-solid-state rechargeable battery, ACS Appl. Mater. Interfaces 9 (2017) 19870—19880, https://doi.org/10.1021/acsami.7b041 12. J.
59. Ou, Y. Zhang, L. Chen, H. Yuan, D. Xiao, Heteroatom doped porous carbon derived from hair as an anode with high performance for lithium ion batteries, RSC Adv. 4 (2014) 63784—63791, https://doi.org/10.1039/C4RA12121J.
60. M. Brebu, I. Spiridon, Thermal degradation of keratin waste, J. Anal. Appl. Pyrolysis 91 (2011) 288—295, https://doi.org/10.1016/j.jaap.201 1.03.003.
61. A.M. Abioye, F.N. Ani, Recent development in the production of activated carbon electrodes from agricultural waste biomass for supercapacitors: a review, Renew. Sustain. Energy Rev. 52 (2015) 1282—1293, https://doi.org/ 10.1016/j.rser.2015.07.129.
62. M. Molina-Sabio, F. Rodriguez-Reinoso, Role of chemical activation in the development of carbon porosity, Colloids Surf. A Physicochem. Eng. Asp. 241 (2004) 15—25, https://doi.org/10.1016/j.colsurfa.2004.04.007.
63. H.M. Coromina, D.A. Walsh, R. Mokaya, Biomass-derived activated carbon with simultaneously enhanced CO2 uptake for both pre and post combustion capture

applications, J. Mater. Chem. A. 4 (2016) 280—289, https://doi.org/10.1039/C5TA09202G.
64. Z. Fan, Y. Liu, J. Yan, G. Ning, Q. Wang, T. Wei, L. Zhi, F. Wei, Template-directed synthesis of pillared-porous carbon nanosheet architectures: highperformance electrode materials for supercapacitors, Adv. Energy Mater. 2 (2012) 419—424, https://doi.org/10.1002/aenm.201 100654.
65. H. Xu, J. Chen, D. Wang, Z. Sun, P. Zhang, Y. Zhang, X. Guo, Hierarchically porous carbon-coated SnO2@graphene foams as anodes for lithium ion storage, Carbon (2017), https://doi.org/10.1016/j.carbon.2017.09.016.
66. Z. Chen, X. Wang, B. Xue, W. Li, Z. Ding, X. Yang, J. Qiu, Z. Wang, Rice huskbased hierarchical porous carbon for high performance supercapacitors: the structure-performance relationship, Carbon (2020), https://doi.org/10.1016/j.carbon.2020.01.088.
67. N. Shimodaira, A. Masui, Raman spectroscopic investigations of activated carbon materials, J. Appl. Phys. 92 (2002) 902—909, https://doi.org/10.1063/ 1.1487434.
68. E. Senoz, R.P. Wool, C.W.J. McChalicher, C.K. Hong, Physical and chemical changes in feather keratin during pyrolysis, Polym. Degrad. Stabil. 97 (2012) 297-307, https://doi.org/10.1016/j.polymdegradstab.2011.12.018.
69. P. Sun, Z.-T. Liu, Z.-W. Liu, Particles from bird feather: a novel application of an ionic liquid and waste resource, J. Hazard Mater. 170 (2009) 786—790, https://doi.org/10.1016/j.jhazmat.2009.05.034.
70. X. Jiao, Y. Qiu, L. Zhang, X. Zhang, Comparison of the characteristic properties of reduced graphene oxides synthesized from natural graphites with different graphitization degrees, RSC Adv. 7 (2017) 52337-52344, https://doi.org/10.1039/C7RA10809E.
71. A.P. Terzyk, The influence of activated carbon surface chemical composition on the adsorption of acetaminophen (paracetamol) in vitro. Part II. TG, FTIR, and XPS analysis of carbons and the temperature dependence of adsorption kinetics at the neutral pH, Colloids Surf. A Physicochem. Eng. Asp. 177 (2001) 23—45, https://doi.org/10.1016/S0927-7757(00)00594-X.
72. M. Hao, N. Xiao, Y. Wang, H. Li, Y. Zhou, C. Liu, J. Qiu, Pitch-derived N-doped porous carbon nanosheets with expanded interlayer distance as highperformance sodium-ion battery anodes, Fuel Process, Technol. 177 (2018) 328—335, https://doi.org/10.1016/j.fuproc.2018.05.007.
73. K. Wang, N. Zhao, S. Lei, R. Yan, X. Tian, J. Wang, Y. Song, D. Xu, Q. Guo, L. Liu, Promising biomass-based activated carbons derived from willow catkins for high performance supercapacitors, Electrochim. Acta 166 (2015) 1—11, https://doi.org/10.1016/j.electacta.2015.03.048.
74. M. Fu, W. Chen, X. Zhu, B. Yang, Q. Liu, Crab shell derived multi-hierarchical carbon materials as a typical recycling of waste for high performance supercapacitors, Carbon 141 (2019) 748-757, _ https://doi.org/10.1016/ j.carbon.2018.10.034.
75. Y. Li, S. Liu, Y. Liang, Y. Xiao, H. Dong, M. Zheng, H. Hu, Y. Liu, Bark-based 3D porous carbon nanosheet with ultrahigh surface area for high performance supercapacitor

electrode material, ACS Sustain. Chem. Eng. 7 (2019) 13827-13835, https://doi.org/10.1021/acssuschemeng.9b01779.
76. W. Yu, H. Wang, S. Liu, N. Mao, X. Liu, J. Shi, W. Liu, S. Chen, X. Wang, N, Ocodoped hierarchical porous carbons derived from algae for high-capacity supercapacitors and battery anodes, J. Mater. Chem. A. 4 (2016) 5973—5983, https://doi.org/10.1039/C6TA01821A.
77. W. Tian, Q. Gao, Y. Tan, K. Yang, L. Zhu, C. Yang, H. Zhang, Bio-inspired beehive-like hierarchical nanoporous carbon derived from bamboo-based industrial by-product as a high performance supercapacitor electrode material, J. Mater. Chem. A. 3 (2015) 5656—5664, https://doi.org/10.1039/CA4TA06620K.
78. L. Jiang, L. Sheng, X. Chen, T. Wei, Z. Fan, Construction of nitrogen-doped porous carbon buildings using interconnected ultra-small carbon nanosheets for ultra-high rate supercapacitors, J. Mater. Chem. A. 4 (2016) 11388-11396, https://doi.org/10.1039/C6TA02570F.
79. T.K. Enock, C.K. King'ondu, A. Pogrebnoi, Y.A.C. Jande, Status of biomass derived carbon materials for supercapacitor application, Int. J. Electrochem. (2017) 1—14, https://doi.org/10.1155/2017/6453420, 2017.
80. D. He, J. Niu, M. Dou, J. Ji, Y. Huang, F. Wang, Nitrogen and oxygen co-doped carbon networks with a mesopore-dominant hierarchical porosity for high energy and power density supercapacitors, Electrochim. Acta 238 (2017) 310-318, https://doi.org/10.1016/j.electacta.2017.03.218.
81. M. Hillion, H. Antelmann, Thiol-based redox switches in prokaryotes, Biol. Chem. 396 (2015) 415—444, https://doi.org/10.1515/hsz-2015-0102.
82. R. Lohmayer, A. Kappler, T. Losekann-Behrens, B. Planer-Friedrich, Sulfur species as redox partners and electron shuttles for ferrihydrite reduction by Sulfurospirillum deleyianum, Appl. Environ. Microbiol. 80 (2014) 3141—3149, https://doi.org/10.1128/AEM.04220-13.
83. H. Feng, M. Zheng, H. Dong, Y. Xiao, H. Hu, Z. Sun, C. Long, Y. Cai, X. Zhao, H. Zhang, B. Lei, Y. Liu, Three-dimensional honeycomb-like hierarchically structured carbon for high-performance supercapacitors derived from highash-content sewage sludge, J. Mater. Chem. A. 3 (2015) 15225-15234, https://doi.org/10.1039/c5ta03217b.
84. D. Pech, M. Brunet, H. Durou, P. Huang, V. Mochalin, Y. Gogotsi, P.-L. Taberna, P. Simon, Ultrahigh-power micrometre-sized supercapacitors based on onionlike carbon, Nat. Nanotechnol. 5 (2010) 651—654, https://doi.org/10.1038/ nnano.2010.162.
85. C. Peng, X. Bin Yan, R.T. Wang, J.W. Lang, Y.J. Ou, Q.J. Xue, Promising activated carbons derived from waste tea-leaves and their application in high performance supercapacitors electrodes, Electrochim. Acta 87 (2013) 401—408, https://doi.org/10.1016/j.electacta.2012.09.082.
86. R. Manikandan, C.J. Raj, M. Rajesh, B.C. Kim, J.Y. Sim, K.H. Yu, Electrochemical behaviour of lithium, sodium and potassium ion electrolytes in a Nag33V205 symmetric pseudocapacitor with high performance and high cyclic stability, ChemElectroChem 5 (2018) 101-111, https://doi.org/10.1002/ celc.201700923.

87. F. Béguin, E. Frackowiak, Supercapacitors, Wiley-VCH Verlag GmbH & Co. KGaA, Weinheim, Germany, 2013, https://doi.org/10.1002/9783527646661.
88. D. Guo, X. Song, B. Li, L. Tan, H. Ma, H. Pang, X. Wang, L. Zhang, D. Chu, Oxygen enriched carbon with hierarchical porous structure derived from biomass waste for high-performance symmetric supercapacitor with decent specific capacity, J. Electroanal. Chem. (2019) 113349, https://doi.org/10.1016/ jjelechem.2019.113349.
89. C. Long, L. Jiang, X. Wu, Y. Jiang, D. Yang, C. Wang, T. Wei, Z. Fan, Facile synthesis of functionalized porous carbon with three-dimensional interconnected pore structure for high volumetric performance supercapacitors, Carbon 93 (2015) 412—420, https://doi.org/10.1016/j.carbon.2015.05.040.
90. W. Huang, H. Zhang, Y. Huang, W. Wang, S. Wei, Hierarchical porous carbon obtained from animal bone and evaluation in electric double-layer capacitors, Carbon 49 (2011) 838—843, https://doi.org/10.1016/j.carbon.2010.10.025.
91. X. He, P. Ling, M. Yu, X. Wang, X. Zhang, M. Zheng, Rice husk-derived porous carbons with high capacitance by ZnClz activation for supercapacitors, Electrochim. Acta 105 (2013) 635-641, https://doi.org/10.1016/ j.electacta.2013.05.050.
92. E.Y.L. Teo, L. Muniandy, E.-P. Ng, F. Adam, A.R. Mohamed, R. Jose, K.F. Chong, High surface area activated carbon from rice husk as a high performance supercapacitor electrode, Electrochim. Acta 192 (2016) 110—119, https:// doi.org/10.1016/j.electacta.2016.01.140.
93. C. Chen, Y. Zhang, Y. Li, J. Dai, J. Song, Y. Yao, Y. Gong, I. Kierzewski, J. Xie, L. Hu, All-wood, low tortuosity, aqueous, biodegradable supercapacitors with ultrahigh capacitance, Energy Environ. Sci. 10 (2017) 538—545, https://doi.org/ 10.1039/C6EE037 16].
94. H. Feng, H. Hu, H. Dong, Y. Xiao, Y. Cai, B. Lei, Y. Liu, M. Zheng, Hierarchical structured carbon derived from bagasse wastes: a simple and efficient synthesis route and its improved electrochemical properties for highperformance supercapacitors, J. Power Sources 302 (2016) 164—173, https:// doi.org/10.1016/j.jpowsour.2015.10.063.
95. D. Wang, G. Fang, T. Xue, J. Ma, G. Geng, A melt route for the synthesis of activated carbon derived from carton box for high performance symmetric supercapacitor applications, J. Power Sources 307 (2016) 401—409, https:// doi.org/10.1016/j.jpowsour.2016.01.009.
96. A. Yadav, B. De, S.K. Singh, P. Sinha, K.K. Kar, Facile development strategy of a single carbon-fiber-based all-solid-state flexible lithium-ion battery for wearable electronics, ACS Appl. Mater. Interfaces 11 (2019) 7974—7980, https://doi.org/10.1021/acsami.8b20233.